

# The Optical Two and Three-Dimensional Fundamental Plane Correlations for More than 180 Gamma-Ray Burst Afterglows with *Swift*/UVOT, RATIR, and the SUBARU Telescope

M.G. DAINOTTI,<sup>1, 2, 3, 4</sup> S. YOUNG,<sup>5</sup> L. LI,<sup>6</sup> K. K. KALINOWSKI,<sup>7</sup> DELINA LEVINE,<sup>8</sup> D. A. KANN,<sup>9</sup> BRANDON TRAN,<sup>10</sup>  
L. ZAMBRANO-TAPIA,<sup>11</sup> A. ZAMBRANO-TAPIA,<sup>11</sup> B. CENKO,<sup>12, 13</sup> M. FUENTES,<sup>11</sup> E. G. SÁNCHEZ-VÁZQUEZ,<sup>14</sup>  
S. OATES,<sup>15</sup> N. FRAJIA,<sup>16</sup> R. L. BECERRA,<sup>17</sup> A. M. WATSON,<sup>16</sup> N. R. BUTLER,<sup>18</sup> J. J. GONZÁLEZ,<sup>16</sup>  
A. S. KUTYREV,<sup>19, 20</sup> W. H. LEE,<sup>16</sup> J. X. PROCHASKA,<sup>21</sup> E. RAMIREZ-RUIZ,<sup>22</sup> M. G. RICHER,<sup>23</sup> AND S. ZOLA<sup>24</sup>

<sup>1</sup>*Division of Science, National Astronomical Observatory of Japan, 2-21-1 Osawa, Mitaka, Tokyo 181-8588, Japan;  
maria.dainotti@nao.ac.jp*

<sup>2</sup>*The Graduate University for Advanced Studies (SOKENDAI), 2-21-1 Osawa, Mitaka, Tokyo 181-8588, Japan*

<sup>3</sup>*Space Science Institute, 4750 Walnut Street, Boulder, CO 80301, USA*

<sup>4</sup>*SLAC National Accelerator Laboratory, 2575 Sand Hill Road, Menlo Park, CA 94025, USA*

<sup>5</sup>*Department of Physics and Astronomy, University of Pennsylvania, 209 South 33rd Street, Philadelphia, PA 19104, USA;  
youngsam@sas.upenn.edu*

<sup>6</sup>*ICRANet, Piazza della Repubblica 10, I-65122 Pescara, Italy; liang.li@icranet.org*

<sup>7</sup>*Wydział Fizyki, Astronomii i Informatyki Stosowanej, Uniwersytet Jagielloński, ul. Łojasiewicza 11, 30-348 Kraków, Poland*

<sup>8</sup>*University of Maryland, College Park, US*

<sup>9</sup>*Instituto de Astrofísica de Andalucía (IAA-CSIC), Glorieta de la Astronomía s/n, 18008 Granada, Spain*

<sup>10</sup>*Centennial High School, 1820 Rimpau Avenue, Corona, CA 92881, USA*

<sup>11</sup>*Scientific Caribbean Foundation, 12 Camino Francisco Rivera, San Juan, PR 00926, USA*

<sup>12</sup>*Astrophysics Science Division, NASA Goddard Space Flight Center, MC 661, Greenbelt, MD 20771, USA*

<sup>13</sup>*Space Science Institute, 4765 Walnut Street, Boulder, CO 80301, USA*

<sup>14</sup>*Latino Education Advancement Foundation, 210 E Lexington Street, Baltimore MD 21202, USA*

<sup>15</sup>*School of Physics and Astronomy, University of Birmingham, Birmingham B15 2TT, UK*

<sup>16</sup>*Instituto de Astronomía, Universidad Nacional Autónoma de México, Apartado Postal 70-264, 04510 México, CDMX, Mexico*

<sup>17</sup>*Instituto de Ciencias Nucleares, Universidad Nacional Autónoma de México, Apartado Postal 70-264, 04510 México, CDMX, Mexico*

<sup>18</sup>*School of Earth and Space Exploration, Arizona State University, Tempe, AZ 85287, USA*

<sup>19</sup>*Department of Astronomy, University of Maryland, College Park, MD 20742-4111, USA*

<sup>20</sup>*Astrophysics Science Division, NASA Goddard Space Flight Center, 8800 Greenbelt Road, Greenbelt, MD 20771, USA*

<sup>21</sup>*Department of Astronomy and Astrophysics, UCO/Lick Observatory, University of California, 1156 High Street, Santa Cruz, CA 95064, USA*

<sup>22</sup>*Department of Astronomy, University of California, Berkeley, CA 94720-3411, USA*

<sup>23</sup>*Instituto de Astronomía, Universidad Nacional Autónoma de México, Unidad Académica en Ensenada, 22860 Ensenada, BC, Mexico*

<sup>24</sup>*Astronomical Observatory, Jagiellonian University, ul. Orła 271, 30-244 Kraków, Poland*

## ABSTRACT

Gamma-ray bursts (GRBs) are fascinating events due to their panchromatic nature. We study optical plateaus in GRB afterglows via an extended search into archival data. We comprehensively analyze all published GRBs with known redshifts and optical plateaus observed by many ground-based telescopes (e.g., Subaru Telescope, RATIR) around the world and several space-based observatories such as the *Neil Gehrels Swift Observatory*. We fit 502 optical light curves (LCs), showing the existence of the plateau in 181 cases. This sample is 77% larger than the previous one (Dainotti et al. 2021a), and it is the largest compilation so far of optical plateaus. We discover the 3D fundamental plane relation at optical wavelengths using this sample. This correlation is between the rest-frame time at the end of the plateau emission,  $T_{\text{opt}}^*$ , its optical luminosity,  $L_{\text{opt}}$ , and the peak in the optical prompt emission,  $L_{\text{peak, opt}}$ , thus resembling the three-dimensional (3D) X-ray fundamental plane relation (Dainotti et al. 2016). We correct our sample for redshift evolution and selection effects, discovering that this correlation is indeed intrinsic to GRB physics. We investigate the rest-frame end time distributions in X-rays

and optical ( $T_{\text{opt}}^*$ ,  $T_X^*$ ), and conclude that the plateau is achromatic only when selection biases are not considered. We also investigate if the 3D optical correlation may be a new discriminant between optical GRB classes and **find that there is no significant separation between the classes compared to the Gold sample plane after correcting for evolution.**

## 1. INTRODUCTION

Gamma-Ray Bursts (GRBs), among the most luminous phenomena in the Universe, originate from the deaths of massive stars (Woosley 1993a; Paczyński 1998; Woosley and Bloom 2006; Cano et al. 2017) or the merging of two compact objects, like neutron stars (NSs; Duncan and Thompson 1992; Usov 1992; Thompson 1994; Metzger et al. 2011) and black holes (BHs, Narayan et al. 1992). These models can have **hyper-accreting BHs** or fast-spinning newly born highly-magnetized NSs (magnetars) as central engines.

To distinguish the different origins, we categorize GRBs according to their phenomenology. The GRB prompt emission is observed from hard X-rays to  $\geq 100$  MeV  $\gamma$ -rays, and sometimes also in the optical (Vestrand et al. 2005; Blake et al. 2005; Beskin et al. 2010). The afterglow (e.g., Costa et al. 1997; van Paradijs et al. 1997; Piro et al. 1998; Gehrels et al. 2009; Wang et al. 2015) is the long-lasting multi-wavelength emission (in X-rays, optical, and sometimes radio) following the prompt.

GRBs are traditionally **further** classified as Short (SGRBs) and Long GRBs (LGRBs), depending on their duration:  $T_{90} \leq 2$  s or  $T_{90} \geq 2$  s,<sup>1</sup> respectively (Mazets et al. 1981; Kouveliotou et al. 1993). Zhang et al. (2009) proposed a classification based on the GRBs' progenitors, according to which GRBs are divided in Type I/II, see Fig. 8 in Zhang et al. (2009) and Kann et al. (2011) for a discussion of controversial cases. Type II GRBs originate from the collapse of massive stars (Woosley 1993b). These include LGRBs, X-ray flashes (XRFs) with soft spectra and greater fluence in X-rays (2-30 keV) than in  $\gamma$ -rays (30-400 keV, Heise et al. (2001)), Ultra-Long GRBs (ULGRBs) with  $T_{90} > 1000$  s (Gendre et al. 2013; Levan et al. 2014; Piro et al. 2014; Greiner et al. 2015; Kann et al. 2018; Gendre et al. 2019), and GRBs associated with SNe Ic. GRB-SNe Ic are **further** classified in A, B, C, D, and E classes (Hjorth et al. 2003). The A, B, and C classes, which are more spectroscopically associated with SNe, are used in this work, hereafter denoted as GRB-SNe ABC. Type I GRBs, resulting from the mergers of compact objects (Abbott et al. 2017a,b), include SGRBs, SGRBs with extended emission (SEEs, Norris and Bonnell 2006; Levan et al. 2007; Norris et al. 2010; Dichiara et al. 2021) and the intrinsically short (IS), namely Short in the rest frame with  $T_{90}^* = T_{90}/(1+z) < 2$  s (Levesque et al. 2010; Ahumada et al. 2021; Zhang et al. 2021; Rossi et al. 2021). Here, we use SGRBs, which include both SEEs and ISs as a unique class.

Observations of the X-ray afterglows performed by the *Neil Gehrels Swift Observatory* (*Swift*) revealed the presence of an X-ray plateau (O'Brien et al. 2006; Sakamoto et al. 2007; Evans et al. 2009; Zhang et al. 2006; Nousek et al. 2006). This phase generally lasts from  $10^2$  s to  $10^3$  s and is followed by a power law (PL) decay phase. The plateau can be explained with the long-lasting energy injection from the central engine by fallback mass accretion onto a BH (Kumar et al. 2008; Cannizzo and Gehrels 2009; Cannizzo et al. 2011) or with the energy injection produced by the spin-down luminosity of a highly magnetized millisecond newborn NS, a magnetar (e.g., Duncan and Thompson 1992; Usov 1992; Thompson 1994; Dai and Lu 1998; Zhang and Mészáros 2001; Troja et al. 2007; Metzger et al. 2011; Dall'Osso et al. 2011; Rowlinson et al. 2014; Rea et al. 2015; Li et al. 2018b; Stratta et al. 2018; Metzger 2019; Fraija et al. 2020). The plateau found in X-rays and optical has been identified as a trait that may standardize GRBs. Dainotti et al. (2016, 2017b); Dainotti and Del Vecchio (2017) and Li et al. (2018b) explored the luminosity at the end of the plateau,  $L_{X,a}$  vs. its the rest-frame time  $T_{X,a}^*$  (known as the Dainotti relation or 2D L-T relation), with the rest-frame time denoted with an asterisk. Rowlinson et al. (2014) showed that the Dainotti relation in X-rays is recovered within the magnetar scenario with a slope for  $L_a$ - $T_{X,a}^*$  of  $-1$ . Within the cosmological context, this correlation has already been applied to construct a GRB Hubble diagram out to  $z > 8$  (Cardone et al. 2009, 2010; Postnikov et al. 2014; Dainotti et al. 2013).

As pointed out in Dainotti et al. (2008, 2010, 2016, 2017b,a), to obtain a class of GRBs that can be well-standardized, we need to select a GRB sub-sample with well-defined properties from a morphological or physical point of view. Thus, we segregate each class in GRBs-SNe Ic, XRFs, X-ray Rich (XRR; an intermediate case between the LGRBs and XRFs), UL, SGRBs, SEE, IS GRBs, and LGRBs, all of which are defined as the total sample from which we remove all other classes. **Regarding the connection between prompt and plateau emission, we annotate the peak prompt luminosity in 1 second,  $L_{X,peak}$  vs.  $T_{X,a}^*$  correlation. A theoretical interpretation of this correlation is**

<sup>1</sup>  $T_{90}$  is the time over which a burst emits from 5% to 95% of its prompt emission total measured counts.

within the standard fireball model and with the changing of the microphysical parameters (van Eerten 2014b,a). An extension of the 2D L-T relation has been obtained by adding the peak prompt luminosity,  $L_{X,peak}$  leading to the so-called Dainotti 3D relation (Dainotti et al. 2016, 2017b, 2020a). We enhance the previous definition of Gold GRBs from Dainotti et al. (2016) with new criteria: identifying the plateaus with fewer gaps in the data points and with more minor fluctuations in the fluxes. The criteria guarantee a tighter correlation involving the plateau emission to use it as a future cosmological tool and a theoretical model discriminator.

In this work, we investigate (1) the 3D Dainotti relation in optical; (2) the 3D optical correlation as a discriminant between GRB classes; (3) the 2D optical correlation with our incremented sample size to determine **if it can be a discriminant among classes**; and (4) if with a larger sample and with the correction for selection biases, whether the plateau is an achromatic feature between X-rays and optical.

In §2, we describe the sample. In §3, we show how we corrected for Galactic and host-galaxy extinction and fitted our sample. In §4, we present the 2- and 3D optical Dainotti relations, also corrected for selection biases and redshift evolution. We discuss our conclusions in §6.

## 2. SAMPLE SELECTION

We analyzed 502 GRB optical afterglows with known redshifts, thus building the most comprehensive sample of optical LCs to date by searching the literature for all GRBs detected between 1997 May and 2021 May by several satellites (e.g., the *Swift* Ultraviolet/Optical Telescope (UVOT)), and ground-based telescopes/detectors, e.g., the Subaru Telescope, Gamma-ray Burst Optical/Near-IR Detector (GROND), Re-ionization and Transients InfraRed camera/telescope (RATIR), the MITSune, etc. In our final sample, the redshifts span from  $z = 0.06$  to  $z = 8.23$  and the LCs are taken from Kann et al. (2006, 2010, 2011, 2021a, 2021b in preparation), Li et al. (2012, 2015, 2018a), Oates et al. (2009, 2012), Zaninoni et al. (2013); Si et al. (2018), the RATIR collaboration, the GCN Circular Archive (GCN)<sup>2</sup>, the *Swift* Burst Analyzer (Evans et al. 2010), and other literature. A table with the GRB name, redshift, fitting parameters, and data source is available in the online supplementary material. Following Dainotti et al. (2021a), we use 68 LCs from Kann et al. (2006, 2010, 2011, 2021a, 2021b in preparation), 24 GRBs from Li et al. (2012, 2015, 2018a, 2022), 3 GRBs from Oates et al. (2009, 2012), 19 GRBs from Zaninoni et al. (2013), and 16 GRBs from Si et al. (2018) which were in turn taken from Li et al. (2012) and Kann et al. (2006). Out of those, we combined the LCs of 5 GRBs from different authors: 2 from Li et al. (2012, 2015), 1 from Kann et al. (2010); Zaninoni et al. (2013), 1 from Kann et al. (2010); Zaninoni et al. (2013); Oates et al. (2009, 2012). Additionally, we gathered 50 LCs from the GCN, *Swift* Burst Analyzer, the RATIR collaboration, and other literature.

We have also investigated GRB data points taken from the SUBARU Telescope, updating previous LCs and improving the fits of the following 18 GRBs: 110422A, 140801A, 140423A, 141121A, 020124A, 110801A, 100513A, 110503A, 980326A, 150413A, 140907A, 180325A, 160131A, 151027A, 160227A, 151029A, 170113A, 140206A.

## 3. METHODOLOGY

We briefly describe the analysis performed on LCs collected by Li et al. (2012, 2015, 2018a), Kann et al. (2006, 2010, 2011), Oates et al. (2012), Zaninoni et al. (2013), Si et al. (2018), and the LCs taken from the GCN. **A flow chart summarizing all the steps of the analysis can be found in Fig. 1.**

We briefly describe the analysis performed on LCs collected by Li et al. (2012, 2015, 2018a), Kann et al. (2006, 2010, 2011), Oates et al. (2012), Zaninoni et al. (2013), Si et al. (2018), and the LCs taken from the GCN. **A flow chart summarizing all the steps of the analysis can be found in Fig. 1.**

### 3.1. Correction for Galactic and host-galaxy extinction

For the GRBs not already corrected for host extinction in the papers cited previously, we computed the extinction factor  $10^{-A_\lambda/2.5}$  in flux density space. For the GRBs taken from Li et al. (2012, 2015, 2018a), we followed Li et al. (2012, 2015, 2018a) to correct for Galactic and for host-galaxy extinction through the extinction parameter  $A_\lambda$ , assuming  $R_v = 3.1$  and the Small Magellanic Cloud (SMC), Milky Way (MW), or Large Magellanic Cloud (LMC) dust models. The flux contribution coming from the host galaxy at very late times ( $\sim 10^6$  s after the GRB trigger) for some GRBs has also been subtracted.

For the GRBs taken from Kann et al. (2006, 2019) we follow Kann et al. (2006, 2019). **More specifically, for each afterglow, the multiband LCs are fit with a single PL, a smoothly broken PL, or a series of these.**

<sup>2</sup> <https://gcn.gsfc.nasa.gov/>

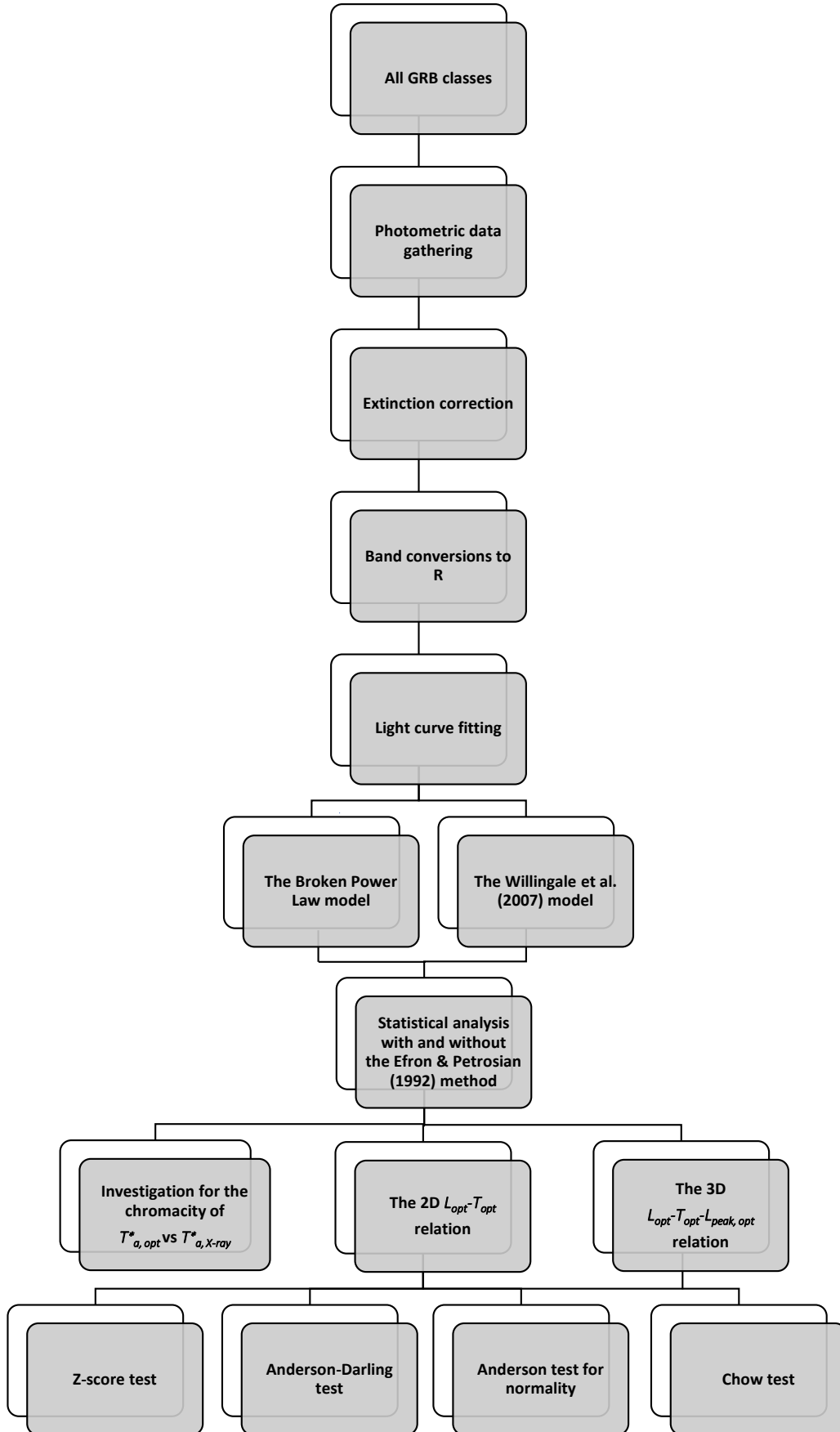


Figure 1. Flow chart summarizing all the steps of the analysis.

If necessary, a constant host-galaxy component is added, and a special supernova-model fit is applied if such an SN is detected (see [Kann et al. 2019](#)). The LCs are corrected for Galactic extinction, and the spectral energy distribution (SED) is assumed to be constant over the region fit and analyzed to determine the line-of-sight extinction from the host galaxy. The SED is then used twofold: first, it allows (after necessary host-and SN-component removal) to shift other bands to the  $R_C$  band, for which there are essentially always measurements, creating a compound LC with maximized data density and temporal coverage. The LCs gathered by [Oates et al. \(2009, 2012\)](#) are corrected for host extinction using the same values as [Oates et al. \(2012\)](#). In [Oates et al. \(2009\)](#), for each GRB, the onset of the prompt  $\gamma$ -ray emission (the start time of the  $T_{90}$  parameter) is equal to the start time of the UVOT LC. However, here we convert it using the Swift Burst Alert Telescope (BAT) trigger time as the start time of the UVOT LCs to have a consistent BAT trigger time, as the other LCs in the sample.

For the LCs gathered from [Zaninoni et al. \(2013\)](#), SEDs are created at early and late times for each GRB, using optical filters for which data were available; spectral index values  $\beta_{opt}$  are derived from fitting these SEDs, corrected for host and Galactic extinction.

For the 50 GRBs gathered from GCNs, we correct for Galactic extinction using the reddening maps from [Schlegel et al. \(1998\)](#), and the  $A_b/E(B - V)_{SFD}$  values from [Schlafly and Finkbeiner \(2011\)](#). For Swift UVOT bandpasses,  $A_b/E(B - V)_{SFD}$  values are taken from the York Extinction Solver [McCall \(2004\)](#).

### 3.2. Magnitude conversions

We converted magnitudes across 18 bandpasses ( $B$ ,  $H$ ,  $I$ ,  $I_C$ ,  $J$ ,  $K$ ,  $K_S$ ,  $R$ ,  $R_C$ ,  $V$ ,  $Z$ ,  $b$ ,  $g$ ,  $i$ ,  $r$ ,  $u$ ,  $v$ , and  $z$ ) into energy fluxes ( $\text{erg cm}^{-2} \text{s}^{-1}$ ) to the  $R$  band using a conversion of zero-point flux densities in any given band and assuming a constant photon index extrapolated from X-ray and taken from [Evans et al. \(2009\)](#) or GCNs. **The formulation for the conversion of flux densities to the R band is the following:**

$$f_R = f_X \left( \frac{\lambda_X}{\lambda_R} \right)^{-\beta}. \quad (1)$$

Then, we can use the following equation to convert from magnitude to flux:

$$F_R = \nu_R f_X \left( \frac{\lambda_X}{\lambda_R} \right)^{-\beta} 10^{-m_X/2.5} \quad (2)$$

where, given a band  $X$ ,  $\lambda_X$  is the effective wavelength ( $\text{\AA}$ ),  $f_X$  the zero-point flux density ( $\text{erg cm}^{-2} \text{s}^{-1} \text{Hz}^{-1}$ ),  $\nu_R$  is the effective frequency (Hz) of the R band in the Johnson-Cousins system,  $m_X$  is the observed magnitude, and  $\beta = \Gamma - 1$ , where  $\Gamma$  is the photon index in X-ray extrapolated taken from [Evans et al. \(2009\)](#) or GCNs. We take effective wavelengths from [Bessell et al. \(1998\)](#) for Johnson-Cousins bands, [Fukugita et al. \(1996\)](#) for SDSS bands, [Poole et al. \(2008\)](#) for *Swift* UVOT bands. Photon index values were taken from GCNs in cases in which the Swift XRT website did not have any photon index for a particular GRB.

Examples of two LCs show data across six band-passes (top left panel of Fig. 2) and an enhanced coverage with data from the Subaru Telescope (top right panel of Fig. 2).

### 3.3. Light curve fitting with the Willingale 2007 (W07) model

We confirm the existence of a plateau by fitting the LCs to the phenomenological [Willingale et al. \(2007\)](#) model (hereafter W07, see the dashed black and solid red lines in Fig. 2).<sup>3</sup> We include all 181 GRBs that can be successfully fitted by the W07 model:

$$f(t) = \begin{cases} F_i \exp \left( \alpha_i \left( 1 - \frac{t}{T_i} \right) \right) \exp \left( -\frac{t_i}{t} \right) & \text{for } t < T_i \\ F_i \left( \frac{t}{T_i} \right)^{-\alpha_i} \exp \left( -\frac{t_i}{t} \right) & \text{for } t \geq T_i, \end{cases} \quad (3)$$

<sup>3</sup> The W07 model makes no assumptions on the underlying physics.

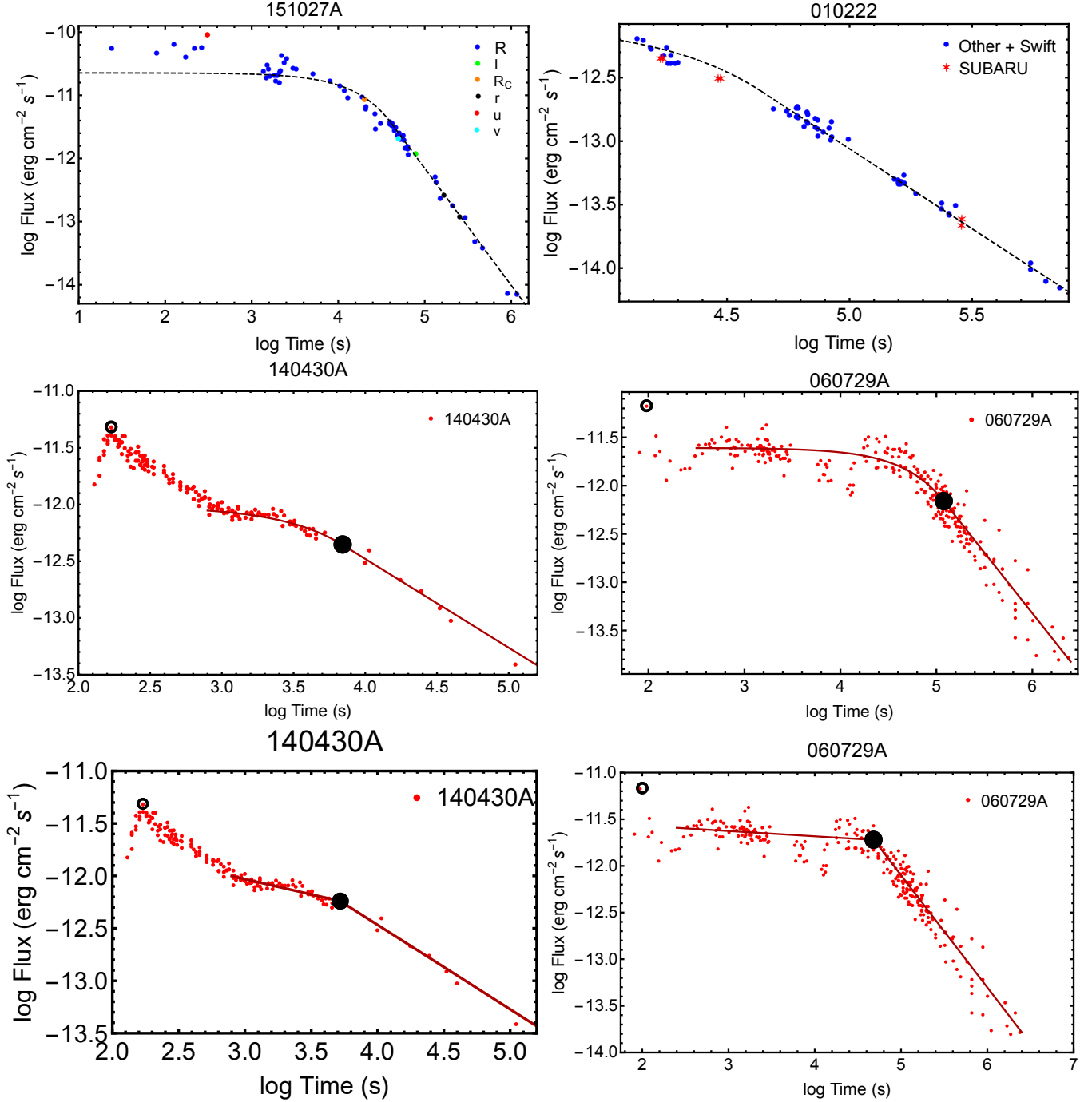


**Figure 2.** The left upper panel shows a LC with multiple bands and the upper right panel shows a LC including the SUBARU data with superimposed the W07 function. The middle panels show examples of the LCs presenting the peak of the prompt emission indicated by an empty black circle and the end of the plateau emission with a filled black circle with superimposed the W07 function with a dark red curve. The bottom panels show the cases of 140430A with the superimposed BPL fit.

where the prompt (index ‘i=p’) and the afterglow (‘i=a’) could be in principle modelled. The LC  $f_{tot}(t) = f_p(t) + f_a(t)$  contains two sets of four free parameters  $(T_i, F_i, \alpha_i, t_i)$ , where  $T_i$  and  $F_i$  are the end times and corresponding fluxes at the plateau end,  $\alpha_i$  is the temporal PL decay index, and  $t_i$  is the initial rise timescale, usually fixed at zero. We exclude cases when the afterglow fitting procedure fails or the determination of  $1\sigma$  confidence intervals does not satisfy the Avni (1976)  $\chi^2$  rules. We show in the middle panel of Fig. 1 two examples of LCs fitted with the W07 model



from a GRB which shows the peak of the prompt emission indicated by an empty red circle. Of the 502 LCs fitted, 181 yield a good fitting. We reject 69 for being a PL, and 42 for not fulfilling the aforementioned  $\Delta\chi^2$  prescriptions, 43 for being too scattered, 148 for having sufficient data points or 19 when multiple reasons above are happening at the same time. **We here clarify that the fit shows the presence of the plateau emission, but we do not require that this fit either W07 or BPL is the only possibility to fit the data.** For the successfully fitted LCs, we compute the source rest-frame isotropic luminosity  $L_{opt}$  (erg s<sup>-1</sup>) at the end of the plateau emission and, when possible, the peak prompt luminosity  $L_{peak, opt}$  (erg s<sup>-1</sup>) following Dainotti et al. (2016, 2017b,a, 2020a, 2021a). The luminosities are defined as follows:

$$L_{opt} = 4\pi D_L^2(z) F_{opt} K, \quad L_{peak, opt} = 4\pi D_L^2(z) F_{peak, opt} K, \quad (4)$$

where  $D_L(z)$  is the luminosity distance assuming a flat  $\Lambda$ CDM cosmological model with  $\Omega_M = 0.3$  and  $H_0 = 70$  km s<sup>-1</sup> Mpc<sup>-1</sup>,  $F_{opt}$  and  $F_{peak, opt}$  are the measured optical energy flux (erg cm<sup>-2</sup> s<sup>-1</sup>) at time  $T_{opt}$ , the end of the plateau, and in the peak of the prompt emission over a one second interval, respectively. Following Bloom et al. (2001), the  $K$ -correction is  $K = 1/(1+z)^{1-\beta_{opt}}$ , where  $\beta$  is the optical spectral index.<sup>4</sup> We use the same  $\beta_{opt}$  for all LCs assuming no spectral evolution. Finally, we construct a sub-sample from the 181 LGRBs called the new gold sample via these morphology conditions:

- The plateau should not be too steep, with an angle of  $< 41^\circ$ . The angle of the plateau is defined as  $\tan^{-1}(\Delta F/\Delta T)$ , with  $\Delta F/\Delta T = (F_i - F_a)/(T_i - T_{opt})$ , where  $i$  denotes the time at the beginning of the plateau.
- The largest change between times in the first 5 consecutive points in the plateau, normalized to the length of the plateau, should be  $(\Delta T/(T_{opt} - T_i))_{\max} < 0.10$ .
- The largest relative change in flux in the first five consecutive points in the plateau should be  $\Delta F_{\max}/F < 0.10$ .

The definition of the  $41^\circ$  comes from Dainotti et al. (2016) in which a Gaussian distribution characterizes the angles; the angles  $> 41^\circ$  are the outliers beyond  $1\sigma$  from that Gaussian. We show the plot of the Gaussian distribution for the X-ray data in Appendix B (Fig. 10) of Dainotti et al. (2017a). To be consistent with the X-ray sample, we use the same definition.

This data quality criterion defines the new Gold Sample, which includes 9 GRBs in the W07 fitting (43% larger than the previous sample of 7). These criteria are chosen such that the definition of the plateau is enhanced, allowing a minimal variation in flux and time while still preserving the existence of the sample; more restrictive criteria would have caused the sample to be smaller, less restrictive criteria would enlarge the sample, but allow larger variation in fluxes and larger gaps in time. Although these criteria may not be the only choices, they safely allow the Gold sample to be reconstructed following these specific criteria. The results of the fitting are stored in Table 2.

### 3.4. Light curve fitting with the simple broken power law model

To give generality to the analysis and to use a model which is not phenomenological and is driven by the underlying physics of the standard fireball model, we have also fitted the 181 sample with the simple broken power law (BPL):

$$f(t) = \begin{cases} F_i \left( \frac{t}{T_i} \right)^{-\alpha_1} & \text{for } t < T_i \\ F_i \left( \frac{t}{T_i} \right)^{-\alpha_2} & \text{for } t \geq T_i, \end{cases} \quad (5)$$

where  $T_i$  is the time at the end of the plateau and  $\alpha_1$  and  $\alpha_2$  are the breaks before and after the plateaus. Within this analysis, we consider the cases that have the angle of the plateau  $< 41^\circ$  corresponding to  $\alpha_1 < 0.8$ . From the analysis of the 181 LCs, we obtain 160 cases that fulfill the requirements of the  $\chi^2$ . For clarity, we present the results of the BPL fitting in Table 3.

Two examples of fitting with the BPL are shown in the bottom panel of Fig. 2. As expected, both the end time of the plateau and its correspondent fluxes are compatible within  $1\sigma$ .

<sup>4</sup> When  $\beta_{opt}$  is not available, we use the XRT index.

## 4. THE OPTICAL CORRELATIONS

We present the results of the fitting with and without evolution for the 2D and 3D correlations using the W07 and the BPL models. We show the z-score values for both models calculated as the distance from the Gold fundamental plane to the other classes (see Table 2 and Table 3). In all plots, all the logarithmic scales are in the base of 10.

4.1. The 3D Fundamental Plane Relation with the Willingale et al. function:  $L_{\text{opt}}^{(l)} - T_{\text{opt}}^{(*,l)} - L_{\text{peak,opt}}^{(l)}$ 

We find that 59 out of the total sample of 181 GRBs show a peak in the prompt emission. To determine the peak flux in these cases, we consider the highest flux before the initial decay phase and when the time is nearly coincident with the peak flux in the X-ray data. Two examples of optical peak fluxes are shown in the bottom panels of Fig. 2. With this information, we build the 3D optical correlation.

The optical fundamental plane relation is defined as:

$$\log L_{\text{opt}} = C_o + a \times \log T_{\text{opt}}^* + b \times \log L_{\text{peak,opt}}, \quad (6)$$

where  $C_o$  is the normalization,  $a_{\text{opt}}$  and  $b_{\text{opt}}$  are the best fit parameters related to  $\log T_{\text{opt}}^*$  and  $\log L_{\text{peak,opt}}$ , respectively, see the upper left panel of Fig. 3. We also consider the evolutionary effects, and we correct for them following Efron and Petrosian (1992). The fundamental plane corrected for selection biases and redshift evolution is:

$$\log L'_{\text{opt}} = C'_o + a' \times \log T'_{\text{opt}} + b' \times \log L'_{\text{peak,opt}}, \quad (7)$$

where  $C'_o$ ,  $a'$  and  $b'$  are the parameters of the plane corrected for selection biases (upper right panel of Fig. 3). The new variables  $L'_{\text{opt}} = L_{\text{opt}}/(1+z)^{k_{\text{opt},L}}$ ,  $L'_{\text{peak,opt}} = L_{\text{peak,opt}}/(1+z)^{k_{\text{opt,peak}}}$  and  $T'_{\text{opt}} = T_{\text{opt}}/(1+z)^{k_{\text{opt},T}}$  where  $k_{\text{opt},L} = 3.96 \pm 0.43$ ,  $k_{\text{opt,peak}} = 3.10 \pm 1.60$  and  $k_{\text{opt},T} = -2.09 \pm 0.40$  define the slope of the evolutionary functions. For details about the application of the method, see Dainotti et al. (2013, 2015, 2017b, 2020a).

**Regarding the X-ray fundamental plane relation, the correction for evolution is  $k_{T_X} = -1.25 \pm 0.28$ , for  $k_{L_X,a} = 2.42 \pm 0.58$ ,  $k_{L_{\text{peak}}} = 2.24 \pm 0.3$ . Thus, the evolutionary parameters for the  $L_a$  and  $k_{T_a}$  are within  $2 \sigma$ , while the  $k_{L_{\text{peak}}}$  is within  $1 \sigma$ .**

The  $a$  parameter between the Gold and all samples are compatible with  $1 \sigma$  both for the corrected and uncorrected variables. The  $b$  and  $C_0$  values of the gold sample, both corrected and uncorrected, are compatible within  $1 \sigma$  with the only exception of the XRFs, which are compatible within  $2 \sigma$ . The last column of Table 2 show the percentage decrease for all samples compared between the uncorrected and corrected correlation in 3D. The intrinsic scatter of the corrected variables as compared to those uncorrected for evolution is smaller by at least 5% in the case of the SNe Ic up to 34% for the XRR GRBs. The only case in which we have an increase of the  $\sigma_{\text{int}}=40\%$  is for the XRFs. However, this result must be taken with a caveat since XRFs are only 4 cases. This shows the importance of accounting for selection biases.

4.2. The 2D Optical Relation with the Willingale et al. (2007) function:  $L_{\text{opt}}^{(l)} - T_{\text{opt}}^{(*,l)}$ 

From Table 2, we see that the slope of the 2D correlation uncorrected for selection biases is compatible within  $1 \sigma$  regardless of the class, except for a few cases. The UL class is compatible in  $2 \sigma$  with GRB-SNe total and GRB-SNe A-B-C, and long. The XRRs have a slope compatible with  $1 \sigma$  with the type I, the XRFs, the UL, and the gold and a slope within  $2 \sigma$  with type II, and with GRB-SNe Ic, GRB-SNe A-B-C and with the LGRBs. The SNe A-B-C are compatible with  $1 \sigma$  with all classes with the exception of UL and XRR. The GRB-SNe all is compatible with  $1 \sigma$  with the exception of the UL, where there is compatibility in  $2 \sigma$  and XRR. The slope of the XRF is compatible with all classes in  $1 \sigma$ . The slope of the gold class is compatible within  $1 \sigma$  with all classes. The type I slope is compatible with  $1 \sigma$  with all classes. The type II slope is compatible with  $1 \sigma$  with all classes except for the XRR.

The normalization constants ( $C_o$ ) are all compatible within  $1 \sigma$  with the exception. The gold  $C_0$  is compatible with all classes. The LGRBs  $C_0$  are compatible with  $1 \sigma$  except for the SNe total and A-B-C and XRR, which are compatible with  $2 \sigma$ . The UL GRBs  $C_0$  is compatible with the one LGRBs, SGRBs, XRR, XRF, Type I and II, and gold in  $1 \sigma$ , and it is compatible within  $2 \sigma$  with the SNe total and SNe-A-B-C. The GRB-SNe-ABC have a  $C_o$  compatible in  $1 \sigma$  with gold, SGRBs, GRB-SNe total, XRFs, type I, while in  $2 \sigma$  with LGRBs, XRRs, ULGRBs and  $3 \sigma$  for type II. The GRB-SNe have a  $C_0$  compatible with  $1 \sigma$  with gold, SGRBs with GRB-SNe-A-B-C, the XRFs, and Type I, while  $2 \sigma$  with LGRBs, ULGRBs, XRRs, Type II. The  $C_0$  for SGRBs is compatible in  $1 \sigma$  with all classes. We



GRB	Author	z	T90 (s)	Class	logFa ( $\text{erg cm}^{-2} \text{s}^{-1}$ )	logFaErr ( $\text{erg cm}^{-2} \text{s}^{-1}$ )	logTa (s)	logTaErr (s)	beta (s)	betaErr (s)	logLumTa ( $\text{erg s}^{-1}$ )	logLumTaErr ( $\text{erg s}^{-1}$ )
020124A	GCN[1]	3.198	45.91	L	-12.78	0.055	4.45	0.07	1.36	0.23	46.40	0.15
050502A	GCN[2]	3.793	20	L	-12.96	0.11	4.08	0.08	0.9	0.10	46.11	0.13
081203A	GCN[3]	2.1	294	L	-13.39	0.14	5.35	0.12	1	0.1	45.13	0.15
090530A	GCN[4]	1.266	48	L	-12.11	0.34	4.89	0.14	0.9	0.13	45.83	0.34
100508A	GCN[5]	0.5201	52	L	-12.88	0.16	4.02	0.39	0.4	0.12	44.04	0.16
100513A	-	4.772	84	L	-13.09	0.17	4.32	0.21	1.2	0.17	46.43	0.21
110422A	GCN[7]	1.77	25.9	L	-12.23	0.13	3.34	0.24	0.8	0.09	46.01	0.13
110503A	-	1.613	10	L	-12.98	0.07	4.72	0.06	0.9	0.06	45.21	0.07
110801A	GCN[9]	1.858	385	XRF-L	-11.82	0.03	4.04	0.03	1	0.10	46.56	0.06
111107A	GCN[10]	2.893	26.6	L-XRF	-12.53	0.24	3.19	0.38	1.1	0.14	46.38	0.25
120907A	GCN[11]	0.97	16.9	L	-12.03	0.08	2.84	0.16	0.8	0.10	45.60	0.08
121128A	GCN[12]	2.2	23.3	L	-11.50	0.125	3.03	0.18	1	0.08	47.06	0.12
130420A	GCN[13]	1.297	123.5	L	-12.87	0.07	4.26	0.10	1.2	0.11	45.20	0.08
140206A	GCN[14]	2.73	93.6	L	-10.90	0.02	2.79	0.06	0.8	0.05	47.80	0.04
140423A	GCN[15]	3.26	134	L	-12.77	0.05	4.18	0.06	1	0.08	46.20	0.07
140801A	GCN[16]	1.32	7	L	-12.79	0.04	4.20	0.05	0.70	0.53	45.11	0.20
140907A	GCN[17]	1.21	79.2	L	-12.43	0.05	4.20	0.07	1.2	0.12	45.56	0.07
141121A	GCN[18]	1.47	549.9	UL	-13.19	0.03	5.71	0.02	0.9	0.12	44.91	0.05
150323A	-	0.593	149.6	L	-13.07	0.06	3.68	0.12	1.1	0.21	44.11	0.07
150413A	GCN[20]	3.139	263.6	L	-12.04	0.03	4.50	0.02	0.77	0.09	46.75	0.07
151027A	GCN[21]	0.81	129.69	L	-11.45	0.02	4.62	0.01	1	0.06	46.04	0.02
160131A	GCN[22]	0.972	325	L	-10.95	0.05	3.83	0.04	1	0.06	46.74	0.05
160227A	-	2.38	316.5	L	-12.58	0.51	4.00	0.58	0.7	0.07	45.91	0.51
160314A	GCN[24]	0.726	8.73	L	-12.57	0.16	2.81	0.38	0.9	0.15	44.77	0.16
160425A	GCN[25]	0.555	304.58	L	-12.48	0.26	3.62	0.43	1.5	0.15	44.71	0.26
160804A	GCN[26]	0.736	144.2	L	-12.97	0.06	4.72	0.08	0.9	0.12	44.39	0.07
161014A	GCN[27]	2.823	18.3	L	-12.68	0.14	3.99	0.16	0.8	0.105	46.03	0.15
161219B	GCN[28]	0.1475	6.94	L-SN-C	-12.78	0.01	6.35	0.01	0.8	0.06	42.98	0.01
170113A	GCN[29]	1.968	20.66	L	-12.04	0.19	3.43	0.19	0.8	0.07	46.31	0.20
170405A	GCN[30]	3.51	164.7	L	-12.76	0.26	4.20	0.18	0.8	0.09	46.16	0.27
170604A	GCN[31]	1.329	26.7	L-XRF	-12.22	0.23	3.77	0.43	0.8	0.08	45.73	0.23
170607A	GCN[32]	0.557	23	L	-11.91	0.02	4.19	0.04	0.9	0.07	45.17	0.03
170714A	GCN[33]	0.793	1000	UL	-13.22	0.26	4.46	0.22	0.9	0.05	44.23	0.26
180115A	GCN[34]	2.487	40.9	L	-11.42	0.39	2.94	0.30	0.9	0.10	47.21	0.39
180205A	GCN[35]	1.409	15.5	L	-12.88	0.02	5.01	0.03	0.9	0.145	45.17	0.06
180325A	GCN[36]	2.248	94.1	L	-12.72	0.07	3.92	0.05	0.8	0.10	45.77	0.09
181010A	GCN[37]	1.39	16.4	L	-12.86	0.28	3.18	0.19	0.9	0.09	45.17	0.28
181201A	GCN[38]	0.45	19.2	L	-11.70	0.03	4.75	0.02	0.8	0.06	45.15	0.03
190627A	GCN[39]	1.942	1.6	S	-12.10	0.05	4.73	0.05	1	0.12	46.33	0.08

**Table 1.** The columns show in order the name of the GRB, the GCN information, the redshift, the  $T_{90}$ , the GRB class, the log of the flux at the end of the plateau emission, its error, the time at the end of the plateau emission, its error, the spectral index of the plateau and its error, the logarithm of the luminosity at the end of the plateau emission and its error.

Best Fit Parameters for Various Subsamples in 2D with the W07 model

Best Fit Parameters for Various Subsamples in 2D with the W07 model													
Uncorrected for Evolution							Corrected for Evolution						
Class	N	$a_{\text{opt}}$	$C_o$	$\sigma_{\text{int}}^2$	z	Chow	$a'_{\text{opt}}$	$C'_o$	$\sigma_{\text{int}}'^2$	z'	Chow	$\Delta\sigma_{\text{int}}^2$	
All GRBs	181	$-0.92 \pm 0.06$	$49.12 \pm 0.24$	$0.78 \pm 0.04$	-0.32	0.94	$-0.74 \pm 0.06$	$47.42 \pm 0.27$	$0.64 \pm 0.03$	0.33	0.95	-18%	
Gold	9	$-0.86 \pm 0.26$	$48.81 \pm 0.95$	$0.69 \pm 0.21$	0.00	0.00	$-0.67 \pm 0.22$	$47.01 \pm 1$	$0.50 \pm 0.19$	0.00	0.00	-28%	
LGRBs	104	$-0.91 \pm 0.07$	$49.15 \pm 0.27$	$0.79 \pm 0.06$	0.24	0.91	$-0.72 \pm 0.08$	$47.45 \pm 0.36$	$0.64 \pm 0.05$	-0.4	0.89	-19%	
SGRBs	13	$-0.79 \pm 0.36$	$48.30 \pm 1.41$	$1.4 \pm 0.31$	0.05	0.80	$-0.59 \pm 0.25$	$46.19 \pm 1.24$	$0.98 \pm 0.24$	0.08	0.89	-30%	
GRB-SNe-Ic	26	$-0.81 \pm 0.10$	$48.00 \pm 0.45$	$0.57 \pm 0.09$	0.14	0.03	$-0.69 \pm 0.15$	$47.00 \pm 0.7$	$0.6 \pm 0.1$	0.13	0.47	+5%	
GRB-SNe-ABC	19	$-0.84 \pm 0.11$	$48.24 \pm 0.47$	$0.46 \pm 0.09$	0.12	0.11	$-0.69 \pm 0.12$	$47.17 \pm 0.58$	$0.47 \pm 0.1$	0.11	0.76	+2%	
ULGRBs	7	$-1.46 \pm 0.46$	$51.42 \pm 2.30$	$1.22 \pm 0.44$	0.02	0.63	$-1.1 \pm 0.34$	$49.17 \pm 1.86$	$0.91 \pm 0.3$	0.09	0.58	-25%	
XRFs	16	$-1.00 \pm 0.19$	$48.78 \pm 0.75$	$0.8 \pm 0.16$	0.46	0.25	$-0.65 \pm 0.18$	$46.6 \pm 0.86$	$0.57 \pm 0.14$	0.39	0.32	-29%	
XRRs	44	$-1.16 \pm 0.11$	$49.95 \pm 0.39$	$0.72 \pm 0.09$	0.14	0.52	$-0.89 \pm 0.09$	$48.08 \pm 0.39$	$0.54 \pm 0.08$	0.57	0.67	-25%	
Type I GRBs	13	$-0.79 \pm 0.26$	$48.52 \pm 1.01$	$1.25 \pm 0.28$	-	-	$-0.59 \pm 0.25$	$46.19 \pm 1.24$	$0.98 \pm 0.24$	0.08	0.89	-22%	
Type II GRBs	173	$-0.95 \pm 0.06$	$49.21 \pm 0.24$	$0.78 \pm 0.04$	0.18	0.90	$-0.75 \pm 0.06$	$47.46 \pm 0.27$	$0.61 \pm 0.04$	0.88	0.93	-22%	

Best Fit Parameters for the Subsamples in 3D

Best Fit Parameters for the Subsamples in 3D													
Uncorrected for Evolution							Corrected for Evolution						
Class	N	$a_{\text{opt}}$	$b_{\text{opt}}$	$C_o$	$\sigma_{\text{int}}^2$	Chow	$a'_{\text{opt}}$	$b'_{\text{opt}}$	$C'_o$	$\sigma_{\text{int}}'^2$	Chow	$\Delta\sigma_{\text{int}}^2$	
All GRBs	58	$-0.84 \pm 0.1$	$0.45 \pm 0.08$	$27.44 \pm 3.76$	$0.53 \pm 0.08$	0.35	$-0.75 \pm 0.1$	$0.3 \pm 0.08$	$33.73 \pm 3.66$	$0.42 \pm 0.07$	0.28	-21%	
Gold	6	$-0.98 \pm 0.25$	$0.43 \pm 0.19$	$29.15 \pm 8.70$	$0.52 \pm 0.31$	0.00	$-0.80 \pm 0.27$	$0.30 \pm 0.17$	$34.13 \pm 7.41$	$0.35 \pm 0.19$	0.0	-33%	
LGRBs	30	$-0.87 \pm 0.13$	$0.45 \pm 0.11$	$27.61 \pm 5.39$	$0.53 \pm 0.10$	0.47	$-0.82 \pm 0.14$	$0.33 \pm 0.11$	$32.53 \pm 5.23$	$0.42 \pm 0.11$	0.34	-21%	
GRB-SNe-Ic	9	$-1.03 \pm 0.23$	$0.17 \pm 0.13$	$41.22 \pm 6.23$	$0.38 \pm 0.13$	0.96	$-1.03 \pm 0.24$	$0.18 \pm 0.12$	$40.45 \pm 5.7$	$0.36 \pm 0.14$	0.86	-5%	
GRB-SNe-ABC	7	$-1.09 \pm 0.25$	$0.23 \pm 0.14$	$38.38 \pm 6.92$	$0.37 \pm 0.15$	0.98	$-0.98 \pm 0.24$	$0.19 \pm 0.12$	$39.93 \pm 5.77$	$0.29 \pm 0.16$	0.70	-22%	
XRFs	4	$-0.75 \pm 0.40$	$0.79 \pm 0.19$	$11.16 \pm 9.55$	$0.45 \pm 0.21$	0.83	$-0.73 \pm 0.45$	$0.59 \pm 0.26$	$20.05 \pm 11.96$	$0.63 \pm 0.44$	0.71	+40%	
XRRs	19	$-0.77 \pm 0.22$	$0.33 \pm 0.18$	$32.75 \pm 8.66$	$0.59 \pm 0.14$	0.27	$-0.67 \pm 0.18$	$0.16 \pm 0.13$	$39.74 \pm 5.86$	$0.39 \pm 0.12$	0.32	-34%	

**Table 2.** The first vertical half of the table (left) shows the GRB classes, the normalization, the slope with their respective errors and the  $\sigma^2$  for each class for the 2D correlation uncorrected for selection biases. The second vertical half of the table (right) show the same variables, but corrected for selection biases (denoted by "prime"). The 6th column shows the  $\delta_o^2$  among the classes of the uncorrected GRBs and the corrected by redshift evolution and selection biases. The seventh and eleventh columns show the z-score for the distribution from the 3D planes from the 3D Gold fundamental plane uncorrected and corrected for redshift evolution, respectively.

Best Fit Parameters for the Subsamples in 2D with the BPL model

Uncorrected for Evolution obtained with the BPL fitting					Corrected for Evolution with the BPL fitting							
Class	N	$a_{\text{opt}}$	$C_o$	$\sigma^2_{\text{int}}$	z	Chow	$a'_{\text{opt}}$	$C'_o$	$\sigma'^2_{\text{int}}$	z'	Chow	$\Delta\sigma^2_{\text{int}}$
All GRBs, $< 41^\circ$	160	$-0.94 \pm 0.07$	$49.17 \pm 0.25$	$0.80 \pm 0.04$	-0.20	0.66	$-0.74 \pm 0.06$	$47.45 \pm 0.28$	$0.63 \pm 0.04$	0.53	-	-21%
Gold	13	$-0.79 \pm 0.20$	$48.80 \pm 0.70$	$0.66 \pm 0.15$	0.00	-	$-0.68 \pm 0.18$	$47.46 \pm 0.75$	$0.57 \pm 0.15$	0.00	-	-14%
LGRBs	89	$-0.90 \pm 0.08$	$49.10 \pm 0.31$	$0.77 \pm 0.06$	0.14	0.93	$-0.71 \pm 0.07$	$47.40 \pm 0.31$	$0.64 \pm 0.05$	-0.11	0.57	-17%
SGRBs	12	$-0.83 \pm 0.40$	$48.62 \pm 1.55$	$1.36 \pm 0.26$	-0.06	0.68	$-0.55 \pm 0.27$	$46.14 \pm 1.35$	$0.99 \pm 0.24$	0.25	0.09	-27%
GRB-SNe-Ic	26	$-0.88 \pm 0.12$	$48.36 \pm 0.50$	$0.61 \pm 0.09$	-0.13	0.01	$-0.73 \pm 0.16$	$47.23 \pm 0.72$	$0.63 \pm 0.11$	0.41	0.17	+3%
GRB-SNe-ABC	19	$-0.89 \pm 0.10$	$48.50 \pm 0.44$	$0.48 \pm 0.09$	-0.11	0.01	$-0.77 \pm 0.13$	$47.55 \pm 0.60$	$0.51 \pm 0.10$	0.35	0.36	+6%
ULGRBs	4	$-1.55 \pm 0.50$	$51.48 \pm 2.38$	$1.14 \pm 0.51$	-0.18	0.06	$-1.50 \pm 0.54$	$51.00 \pm 2.75$	$1.10 \pm 0.52$	0.39	0.11	-4%
XRFs	16	$-0.68 \pm 0.14$	$46.81 \pm 0.65$	$0.52 \pm 0.12$	4.26	0.02	$-0.68 \pm 0.14$	$46.76 \pm 0.67$	$0.51 \pm 0.12$	0.57	0.01	-2%
XRRs	42	$-0.85 \pm 0.12$	$48.08 \pm 0.51$	$0.63 \pm 0.08$	7.01	0.29	$-0.84 \pm 0.12$	$47.94 \pm 0.53$	$0.61 \pm 0.08$	0.44	0.52	-3%
Type I GRBs	12	$-0.83 \pm 0.40$	$48.62 \pm 1.55$	$1.36 \pm 0.26$	-0.06	-	$-0.55 \pm 0.27$	$46.14 \pm 1.35$	$0.99 \pm 0.24$	0.25	-	-27%
Type II GRBs	153	$-0.95 \pm 0.06$	$49.22 \pm 0.22$	$0.78 \pm 0.05$	-0.40	-	$-0.74 \pm 0.06$	$47.47 \pm 0.28$	$0.63 \pm 0.04$	0.42	-	-19%

Best Fit Parameters for the Subsamples in 3D obtained with the BPL fitting

Class	N	Uncorrected for Evolution obtained with BPL fitting					Corrected for Evolution					$\Delta\sigma_{\text{int}}^2$
		$a_{\text{opt}}$	$b_{\text{opt}}$	$C_o$	$\sigma_{\text{int}}^2$	Chow	$a'_{\text{opt}}$	$b'_{\text{opt}}$	$C'_o$	$\sigma_{\text{int}}'^2$	Chow	
Gold	5	$-1.20 \pm 0.63$	$0.47 \pm 0.24$	$27.51 \pm 11.16$	$0.96 \pm 0.60$	—	$-1.16 \pm 0.58$	$0.47 \pm 0.23$	$27.60 \pm 10.76$	$0.84 \pm 0.39$	—	−13%
LGRBs	24	$-0.76 \pm 0.16$	$0.20 \pm 0.10$	$39.24 \pm 5.01$	$0.61 \pm 0.14$	0.72	$-0.62 \pm 0.15$	$0.19 \pm 0.09$	$38.38 \pm 3.91$	$0.44 \pm 0.11$	0.54	−28%
GRB-SNe-Ic	6	$-0.82 \pm 0.14$	$0.12 \pm 0.11$	$42.69 \pm 5.17$	$0.21 \pm 0.13$	0.88	$-0.81 \pm 0.16$	$0.19 \pm 0.12$	$39.17 \pm 5.68$	$0.21 \pm 0.15$	0.39	0%
GRB-SNe-ABC	5	$-0.85 \pm 0.18$	$0.14 \pm 0.12$	$42.11 \pm 5.73$	$0.26 \pm 0.18$	0.83	$-0.86 \pm 0.19$	$0.19 \pm 0.12$	$39.50 \pm 5.69$	$0.23 \pm 0.19$	0.45	−12%
XRRs	9	$-0.84 \pm 0.23$	$0.58 \pm 0.25$	$21.40 \pm 12.48$	$0.61 \pm 0.22$	0.53	$-0.72 \pm 0.19$	$0.33 \pm 0.23$	$32.45 \pm 10.94$	$0.38 \pm 0.19$	0.08	−38%
All GRBs, $< 41^\circ$	36	$-0.87 \pm 0.12$	$0.23 \pm 0.08$	$38.31 \pm 4.05$	$0.58 \pm 0.10$	—	$-0.65 \pm 0.10$	$0.18 \pm 0.07$	$38.90 \pm 3.28$	$0.35 \pm 0.08$	—	−40%

**Table 3.** The first vertical half of the table (left) shows the GRB classes, the normalization, the slope with their respective errors and the  $\sigma^2$  for each class for the 2D correlation uncorrected for selection biases. The second vertical half of the table (right) show the same variables, but corrected for selection biases (denoted by "r"). The 7th column shows the  $\Delta\sigma_{\text{int}}^2$  among the classes of the uncorrected GRBs and the corrected by redshift evolution and selection biases. The 8th and eleventh columns show the z-score for the distribution from the 3D planes from the 3D Gold fundamental plane uncorrected and corrected for redshift evolution, respectively.

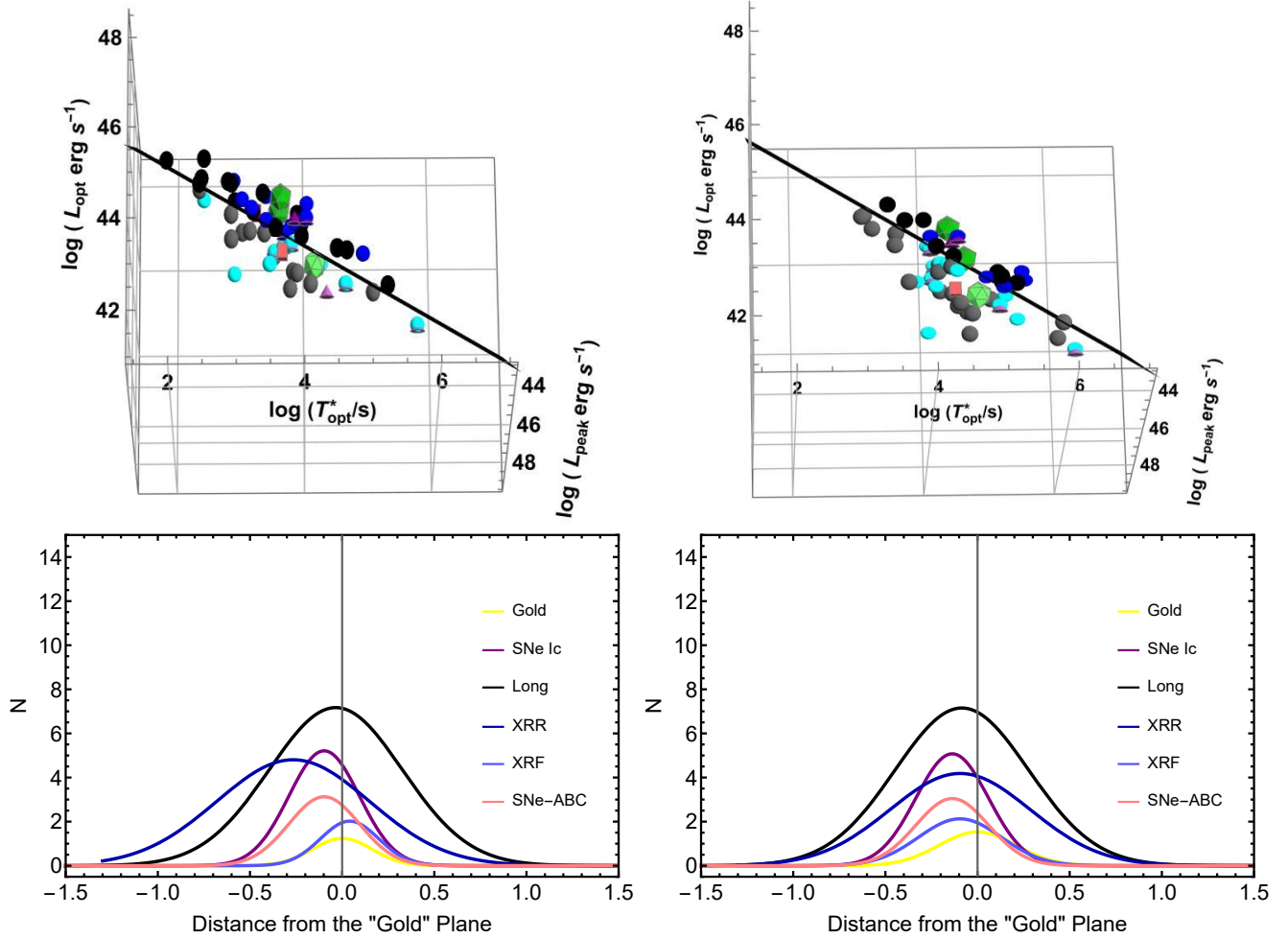


**Figure 3.** Upper panels 59 GRBs in the  $L_{\text{opt}}^{(\prime)} - T_{\text{opt}}^{(*\prime)} - L_{\text{opt}}^{(\prime)}$  parameter space with the fitted plane parameters in Table 2, including LGRBs (black circles), SGRBs (red cuboids), GRB-SNe Ic (purple cones), XRFs and XRRs (blue spheres), and ULGRBs (green icosahedrons). The left and right panels show the 3D correlation with and without any corrections for redshift evolution and selection biases, respectively. Bottom left panel the distances of the GRB of each class indicated with different colors from the Gold fundamental plane, which is taken as a reference. Bottom right panel the same as the bottom left panel, but with correction for evolution.

assume that all classes undergo a similar redshift evolution for simplicity because, besides LGRBs, all other classes have too few GRBs to be considered alone to reliably apply the [Efron and Petrosian \(1992\)](#) method. After corrections for redshift evolution and selection biases, all classes have a slope compatible within  $1 \sigma$ .

The normalizations of the Gold, LGRBs, GRB-SNe total, GRB-SNe-A-B-C, and the UL are compatible within  $1 \sigma$ . The SGRBs  $C_0$  is compatible with  $1 \sigma$  with all classes with the exception of the XRR, which is  $2 \sigma$ . The XRFs are compatible with  $1 \sigma$  all classes with the exception of the XRR, which is compatible with  $2 \sigma$ . The XRRs are compatible within  $2 \sigma$  with XRFs, GRBs-SNe Ic. The slope and normalization of Types I and II, both corrected and uncorrected for selection biases and redshift evolution, are compatible within  $1 \sigma$  mainly due to large error bars on Type I.

This highlights an important finding: the GRB classes are not distinguishable in terms of the parameters of the 2D optical correlation both with and without correction for selection biases and redshift evolution. **The fact that the classes are indistinguishable is checked with the z-score. It is worth noting that the fitting with W07 between the corrected and uncorrected classes provides values of the z-score whose difference among each other is smaller than the difference of the z-score given by the BPL model. This is probably due**

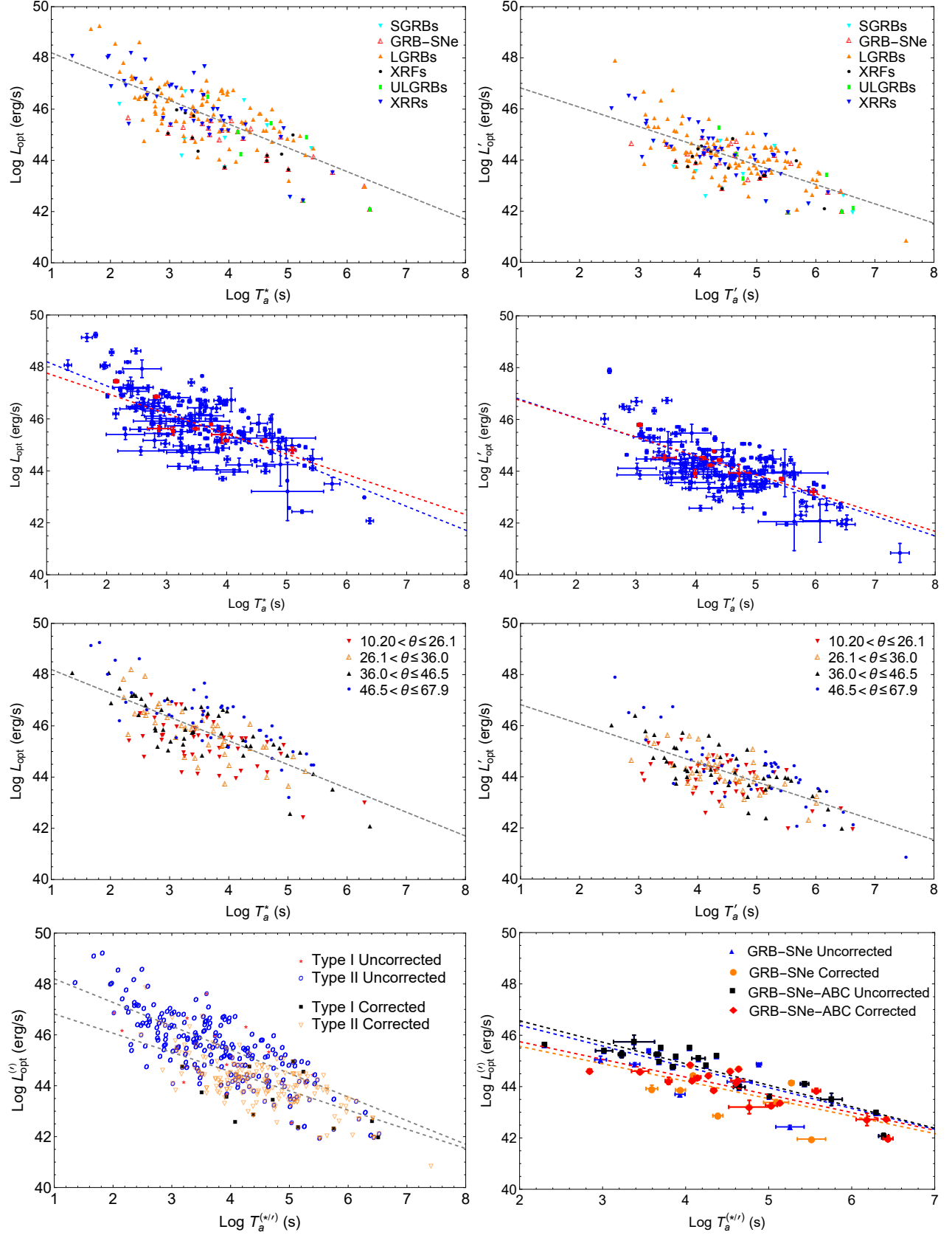


**Figure 4.** The three upper left panels show the observed  $L_{\text{opt}}^{(r)}-T_{\text{opt}}^{(*//)}$  correlations uncorrected for biases and evolution with all classes (first row), the total and Gold samples (second row), and plateau angles (third row), respectively. Panels on the left for the first three rows show the correlation without any correction, on the right with correction. The bottom left panel shows Type I and Type II GRBs. The bottom right shows the GRB-SNe-Ic and GRB-SNe-ABC classes before and after correction.

to the fact that the W07 yields a sample that is 13.1% larger than the BPL sample. This trend is different in the 2D and 3D X-ray correlation, where these classes are distinguishable (Dainotti et al. 2010, 2017b,a, 2020a).

#### 4.3. The 2D and 3D correlation with the BPL function

We repeat the fitting of the selected 181 GRBs with the BPL considering also the requirement that the angle should be less than  $41^\circ$  correspondent to  $\alpha_1 < 0.8$  and we found out that 160 GRBs can be appropriately fitted with a BPL (eq. 2). The results of the fitting both in 2D and in 3D are shown in Table 3.

#### 4.4. The distance from the Gold fundamental plane

Following Dainotti et al. (2021a), we test if the fundamental plane can be a discriminant between classes. Thus, we compute the distance of any GRB class from the plane identified by the Gold sample for both corrected and uncorrected GRBs via a z-score calculation, which is defined as

$$z = \frac{\mu - \mu_{\text{Gold}}}{\sqrt{(\sigma/\sqrt{N})^2 + (\sigma_{\text{Gold}}/\sqrt{N_{\text{Gold}}})^2}}, \quad (8)$$

where  $\mu$  denotes the mean,  $\sigma$  the standard deviation, and  $N$  the number of points in a given sample (see bottom panels of Fig. 3). We find that there is some indication of differences between some classes (with z-scores  $|z^{(i)}| > 1$  in Table 2 and Fig. 3). These classes include XRFs and XRRs in the uncorrected case (the left panels of Fig. 3), but these differences disappear when we consider the correction for evolution (the right panels of Fig. 3). This analysis would benefit from an increased sample, as z-scores are being penalized for rather large *sigmas* and small sample sizes. With a larger sample, we may use the 3D optical fundamental plane as a class discriminator, similarly to the X-ray fundamental plane.

We also test if this total sample of 181 GRBs still holds the same features in terms of the segregation in classes (upper panels of Fig. 4), the presence of the Gold sample (upper-lower panels), and the plateau angles (middle panels). The left panels show the variables without correction for selection biases, while the right panels show correction for evolution. We also investigate if there is clustering in terms of Type I and II GRBs in the bottom left panel and in the case of GRB-SNe Ic (bottom right panel). Similar to Dainotti et al. (2021a), there is no particular clustering of GRBs around any given class, plateau angle, nor within the Gold sample. This occurs within the total sample both with and without the correction for redshift evolution and selection biases. These GRB features are less distinguishable compared to those in X-rays (Dainotti et al. 2021a).

#### 4.5. The Anderson-Darling, Anderson, and Chow tests

We also test if the functional relationship is valid with the Anderson Darling test by checking if  $L_{a,opt}$  is drawn by the same population of the  $L_{opt,theor}$  distribution determined by the plane. In 3D, if we consider the W07 function and the BPL for both the corrected and uncorrected correlation, we find that for both functions, the null hypothesis is heavily favored with  $p > 0.25$  for both the uncorrected and corrected correlations. In two dimensions, we find that the uncorrected correlation in the BPL fitting again favors the null hypothesis at  $p > 0.25$ . In contrast, the corrected correlation accepts the null hypothesis at 15%. When we apply the test with the W07 function, we obtain that the null hypothesis is favored at the 13% level for the uncorrected sample and 16% for the corrected one.

We also applied the Anderson test for normality (or Gaussianity)<sup>5</sup> of residuals applied to the  $(L_{opt,observed} - L_{opt,theor})$ . For both the corrected and uncorrected 3D correlation, fitted with the W07 function, the null hypothesis (that the distribution is drawn from a Gaussian) is accepted at  $p > 15\%$ . For the BPL, the null hypothesis is accepted with  $p > 0.05$  for the uncorrected 3D correlation, and with  $p > 10\%$  for the 3D corrected correlation. For the 2D correlations, all correlations (both corrected and uncorrected for W07 and BPL) are accepted at the  $p > 15\%$  level. Thus, we can safely state that the 2D and 3D correlations in all cases do fulfill both the test of Gaussianity and the Anderson-Darling test for verifying the true nature of the correlation.

<sup>5</sup> The Anderson-Darling and Anderson tests have been performed with `scipy`.



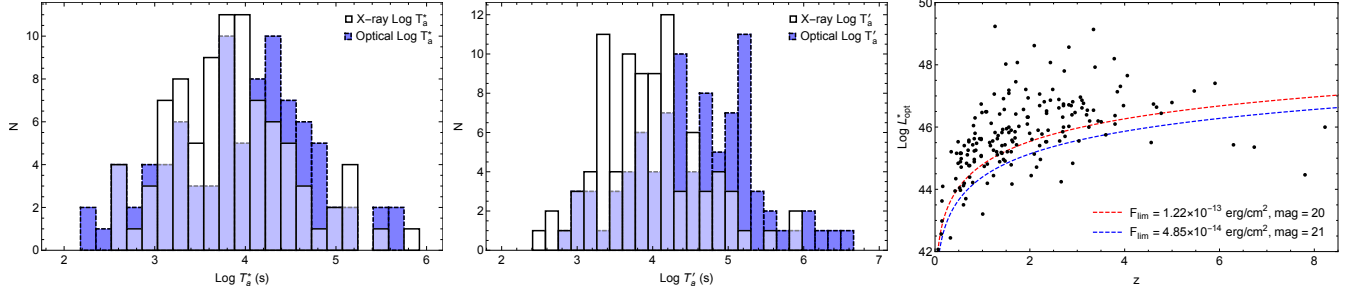


**Figure 5.** Left panel: The differential distribution of  $T_{X,a}^*$  (white solid line) and  $T_{opt,a}^*$  (blue dashed line). Middle panel: The same as the left panel, but corrected for evolution. Right panel: The observed luminosity vs. redshift with limiting luminosity curves given by the observability with Tomo-e Gozen.

Even though we have already presented the values of the z-score in the previous table and this has shown the compatibility among all classes in the 2D and 3D relation, it is worth here to consider additional tests so that we can draw more reliable conclusions. We stress that parameter confidence intervals calculations are based on asymptotic theory. For discussion of multiple regression with small samples, see discussion and references in [Kelley and Maxwell \(2003\)](#). We assume the regression model in Equation 3 is correct. We apply the Chow test to verify whether the true coefficients in two linear regressions on different data sets are equal. Thus, similarly to the z-score test, we take the gold sample as a reference. We compute the Chow test for the several classes against the gold sample both for the cases of the Willingale et al. (2009), the BPL functions in 2D and 3D and for both the cases in which we consider evolution and not evolution. We here discuss first the 2D relation with no evolution. From the Chow test results for the BPL with no evolution we can assess that the gold and long GRBs have the same coefficients with the highest probability of 93% as it is expected because the gold sample is by definition a subclass of long GRBs from which the other classes have been removed. The classes of GRBs associated with the SNe Ic and the SNe A-B-C have both different parameters at 1% ( $p=0.001$ ), and the XRFs yield  $p=0.02$ . The rest of the classes yield similar parameters with  $p > 5\%$ . Interestingly and unexpectedly, the short GRBs have the highest probability of the parameters being similar after the long sample. Regarding BPL cases with evolution, we can state that the results tend to confirm the similarity. All classes show similarity with  $p > 5\%$ , except the XRFs yield  $p=0.01$ . Also, the SNe Ic total sample and the SNe Ic A-B-C after correction show compatibility at the 17% and 36% level, respectively. Interestingly, although the short GRBs still remain compatible with the gold sample, the p-value dropped at 9%. Continuing on the 2D correlation, when we consider the W07 function for the case of no-evolution, the results are comparable with the one with BPL as expected. However, the SNe Ic, differently from the BPL case, shows similar parameters only at 3% level, while the BPL has compatibility only at the 1% for the total SNe Ic and the SNe A-B-C. In the W07 fitting for the case of the SNe A-B-C we have compatibility at the level of 11%. Continuing on the 2D correlation for the W07 function, but with evolution, all classes are compatible with the gold sample, thus showing that also the GRBs associated with SNe Ic becomes compatible. It is interesting to note that although the p-values vary from the BPL and the W07 function, the conclusion of the analysis remains the same, thus supporting the reliability of these conclusions which are independent from the functional forms used for fitting the LCs. Considering the 3D correlation fitted with the BPL, we find that the parameters are all comparable with the gold sample for the cases both with and without evolution.

## 5. COMPARISON BETWEEN OPTICAL AND X-RAYS

### 5.1. Discussion of the current status in the literature

GRB collimation has been inferred with the observations of achromatic steepening in GRB LCs, such steepening are called jet breaks. Pinpointing a jet break from afterglow LCs enables us to measure the jet opening angle and consequently the GRBs' energy. Investigating which GRBs are chromatic and achromatic is crucial tackling this issue. The topic of the achromaticity vs. chromaticity of the LCs in X-rays and optical has been extensively studied in the literature [Panaitescu et al. \(2006\)](#); [Huang et al. \(2006\)](#); [Liang et al. \(2007\)](#); [Molinari et al. \(2007\)](#). To be more specific

in Panaitescu et al. (2006) several GRBs such as 050319, 050401, 050607, 050713A, 050802, and 050922C exhibit a steepening at 1–4 hours in X-rays after the burst, which, surprisingly, is not accompanied by a break in the optical emission. The reason for this behavior is still a puzzling issue. Out of the several GRBs presented in Panaitescu et al. (2006) we have 4 GRBs which are also common to our sample: 050401, 050319, 050802, and 050922C. Most likely, the behavior of not being accompanied by the spectral break does not originate from the outflow collimation. **If the optical and X-ray observations stem from the same synchrotron forward-shock model, we identify the temporal breaks with the passage of the synchrotron cooling break through the X-ray band. That evolution of the synchrotron cooling break depends on the equivalent kinetic energy, circumburst density, microphysical parameters, and the electron population’s spectral index. It is worth noting that a temporal break in the optical observations without observing a temporal break in the X-rays could also be explained by the passage of the spectral break in optical bands.** Liang et al. (2007) analyzed the origin of the shallow X-ray phase in a sample of 53 long bursts detected by Swift. Among the 13 bursts with well-sampled optical LCs, six had an optical break,  $t_b$ , consistent with being achromatic. However, the remaining cases either did not show an optical break or had a break at an epoch different from  $t_b$ . This observational result poses challenges for the synchrotron forward-shock scenario with energy injection, opening up to the possibility that the optical and X-ray emission may not be emitted by the same mechanism, at least for some bursts. There are four significant outliers in the sample, GRBs 060413, 060522, 060607A, and 070110. The last two bursts are also present in our sample. A very steep decay immediately follows the shallow decay phase exhibited in these X-ray lightcurves after  $t_b$ , which is inconsistent with any external shock model. The optical and X-ray observations show that these bursts evolve independently, indicating these X-ray plateaus may have an internal origin.

However, a one to one comparison among the GRBs lightcurves in X-rays and optical results to be more realistic in depicting whether or not we have an achromatic or chromatic plateaus.

In Liang et al. (2007) at least some X-ray breaks are chromatic. In the current paper we check consistency of the chromaticity versus achromaticity scenario for 89 GRBs through GRBs which have both X-ray and optical lightcurves. As a result, we have 13 cases of achromatic emission when we do not correct for selection biases and redshift evolution and 11 cases when we apply these corrections. The achromatic cases, which are a fraction of 14.6% in case of no evolution and 12.3% in case of evolution may reflect that these are associated with an external origin (e.g. refreshed shocks). However, the remaining cases cannot be explained within this scenario.

Invoking different emission regions (e.g., Zhang and Meszaros (2002)) may solve the problem, although more detailed modeling is needed. Crossing a cooling break would also result in a temporal break, but it would also be accompanied by a spectral index variation by  $\sim 0.5$ . Liang et al. (2007) found that the changes in the X-ray spectral indices across the breaks of GRB 050318, 050319, 050802, 050401 are between 0.01 and 0.12, being much smaller than 0.5. Thus, the suggestion of a cooling spectral break is ruled out. Genet et al. (2007) accounted for these chromatic breaks as being due to a long-lived reverse shock in which only a small fraction of the electrons are accelerated. The main issue for such an interpretation is how to “hide” the emission from the forward shock, which carries most of the energy.

Molinari et al. (2007) analyzed the cases of GRB 060418 and GRB 060607A concluded regarding GRB 060418 that due to the difference between the spectral indices in X-rays,  $\beta_X$ , and Near Infrared,  $\beta_{NIR}$  a different origin for those wavelengths may occur. For the case of GRB 060607 a definite conclusion cannot be reached due to the presence of the flares. Wang et al. (2015, 2018) used a large sample of GRBs that have an optical break consistent with being achromatic in the X-ray band. Their sample includes 99 GRBs from 1997 February to 2015 March that have optical and X-ray LCs for Swift GRBs. These X-ray LCs are consistent with the jet break interpretation. Out of these 99 GRBs, 55 GRBs have temporal and spectral behaviors both before and after the break, consistent with the theoretical predictions of the jet break models, respectively. These include 53 long/soft (Type II) and 2 short/hard (Type I) GRBs.

## 5.2. The analysis in this paper

Because of the above discussions based on a one to one comparison, we follow in this current paper two approaches: the first one is to show the distribution of the sample to study the population as a whole, shown in the left and middle panels of Fig. 5 and the second approach is to perform a one to one analysis in which we show the plot of  $T_X$  vs  $T_{opt}$  to highlight the coincidence of the breaks in Fig. 6.

Following Dainotti et al. (2021a), we test if the rest-frame end times ( $T_a^{(*//)}$ ) of the plateau are achromatic in X-rays and optical.

The left panel of 6 shows the cases without evolution, while the right-hand panel shows the cases with evolution. We have shown the uncertainties as ellipses because they are not independent. We also show two examples of the LC comparison between X-ray and optical in that figure. We mark  $T_a$  as a vertical lines, denoted in red for X-ray and blue for the optical. Specifically, we show two cases in which the plateau seems chromaticity (the middle panel of Fig. 6) and two cases of achromaticity (lower panel of Fig. 6) within 1 sigma. We then perform the Kolmogorov-Smirnov (KS) Test for the uncorrected  $T_{X,a}^*$  and  $T_{opt,a}^*$  and the corrected  $T_{X,a}^{(*\prime)}$  and  $T_{opt,a}^{(*\prime)}$  distributions. We find that, for times not corrected for evolution or selection biases, the distance among these distributions,  $D$ , is  $D = 0.18$  with a probability that they are drawn by the same parent population  $P = 0.11$ . However, when we correct for selection biases and redshift evolution the null hypothesis is clearly rejected with  $D = 0.34$  and  $P = 7.0 \times 10^{-5}$ , showing that  $T'_a$  is chromatic across X-ray and optical bands, with the observed X-ray breaks happening earlier than those in the optical. This points toward the hypothesis that the end of the plateaus may be associated with an external origin, indicating that the continuous energy injection has finished (e.g., see Lü and Zhang 2014).

We compute the 2D correlation in X-rays for 89 GRBs in common between the X-rays and optical sample, see the left-hand panel of Fig. 7, obtaining  $a_X = -1.17 \pm 0.10$  and  $a_{opt} = -1.01 \pm 0.11$ . After correcting for observational biases and redshift evolution, we find  $a'_X = -0.94 \pm 0.13$  and  $a'_{opt} = -0.78 \pm 0.08$ , see the right-hand panel of Fig. 7. In both cases, the slopes agree within 1  $\sigma$ .

It is clear from this analysis that we need to increase the observations to be able to tell whether the uncorrected end-time distributions are chromatic across X-ray and optical wavelengths. Thus, we will soon start an observational campaign for optical GRB follow-up with Tomo-e Gozen, a wide-field CMOS camera mounted on the 1.05-m KISO Schmidt telescope located in Nagano, Japan (Sako et al. 2018). We show the limiting luminosities of Tomo-e Gozen at each redshift, assuming we can detect at 20 mag with an exposure time of 100 s, corresponding to  $F_{lim} = 1.22 \times 10^{-13}$  erg cm $^{-2}$  s $^{-1}$  (red dashed line in Fig. 5) and with a 21 mag afterglow and an exposure time of 1000 s, corresponding to  $F_{lim} = 4.85 \times 10^{-14}$  erg cm $^{-2}$ s $^{-1}$  (blue dashed line in Fig. 5). If we consider our sample with redshift with an exposure of 1000 s or more, we can observe a majority of bursts with plateau emission. We have also initiated an international collaboration with DDOTI (Watson et al. 2016) where we have similar limiting luminosities as the ones from the KISO and the Telescope in Krakow CDK 500 within the Skynet network for joint observations. The limiting luminosities for the Telescope in Krakow is of 18 mag (correspondent to  $F_{lim} = 1.31 \cdot 10^{-12}$  in the V band) when the condition of observations are favorable. Based on the current sample of 181 GRBs, we estimate that with the CDK 500 we will still be able to catch a good fraction of the high luminosity plateaus (36%). The great advantage of this synergy is that the three Telescopes are located in three different part of the world (Europe, Mexico and Japan) thus allowing a good coverage of the GRBs if it is observable in three locations.

## 6. DISCUSSION AND CONCLUSIONS

We have gathered the largest compilation of optical plateaus to date (181 GRBs, 77% larger than the previous sample presented in Dainotti et al. 2020b) and show that the  $L_{opt}^{(\prime)} - T_{opt}^{(*\prime)}$  correlation holds, and is compatible with the previous X-ray sample within 1  $\sigma$  both before and after correcting for redshift evolution and selection biases. We also discover the existence of a 3D optical correlation, an extension of the 2D correlation by adding the peak prompt luminosity,  $L_{peak,opt}$ .

The optical correlation in 3D fitted with W07 model is:

$$\log L_{opt} = (-0.84 \pm 0.10) \log T_{opt}^* + (0.45 \pm 0.08) \log L_{peak} + (27.44 \pm 3.76). \quad (9)$$

with  $\sigma^2 = 0.53 \pm 0.08$ . **For the case of the BPL**  $a = -0.87 \pm 0.12$ ,  $b = 0.23 \pm 0.08$  and  $C_0 = 38.31 \pm 4.05$  and  $\sigma = 0.58 \pm 0.1$ . The 3D correlation fitted with W07 after correcting for selection biases and redshift evolution is:

$$\log L'_{opt} = (-0.75 \pm 0.10) \log T'_{opt} + (0.30 \pm 0.08) \log L'_{peak} + (33.73 \pm 3.66). \quad (10)$$

with  $\sigma_{int}^2 = 0.42 \pm 0.07$ . **The parameters for the BPL for**  $a' = -0.65 \pm 0.1$ ,  $b' = 0.18 \pm 0.07$ ,  $C_0 = 39 \pm 3.28$ ,  $\sigma' = 0.35 \pm 0.08$ . The 3D fundamental plane fitted with W07 for the all sample corrected for evolution has a  $\sigma_{int}^2$  21% smaller than the 3D correlation for the uncorrected sample. When we consider the BPL the reduction of scatter is 40% smaller. The Gold sample fitted with W07 uncorrected for selection biases and redshift evolution has a reduced  $\sigma_{int}^2 = 0.52$ , 2% smaller than the total sample, while the corrected Gold sample has  $\sigma_{int}^2 = 0.35$ , 17% smaller than the corrected total sample.

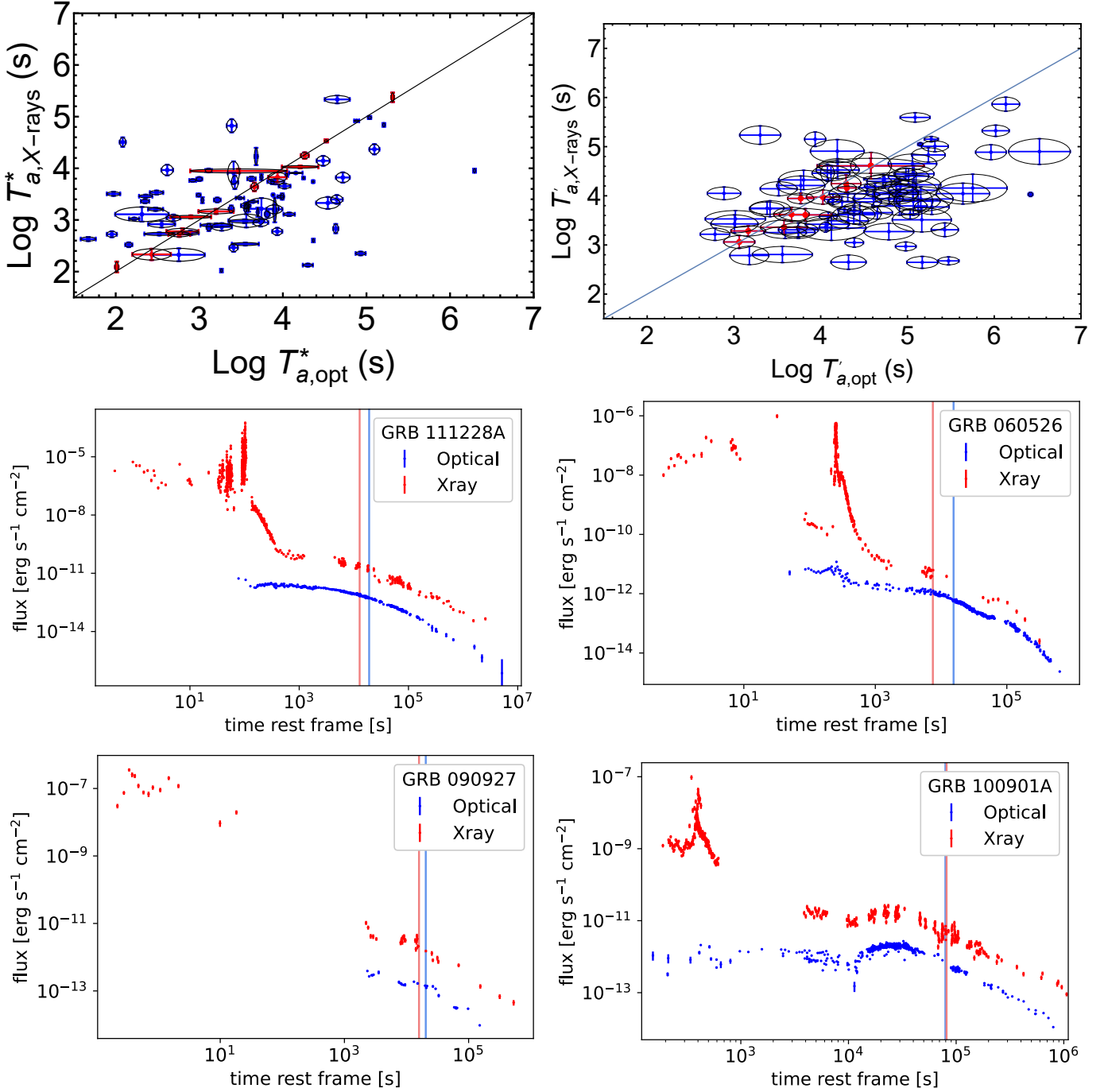


**Figure 6.** Left top panel: plot of  $T_{a,X}$  vs.  $T_{a,opt}$  for uncorrected data. Right top panel: the same plot, but for corrected data. Middle panels: example of GRBs in which the plateau is chromatic in more than  $1 \sigma$  between the X-ray and optical LCs. Lower panels: example of GRBs in which the plateau is achromatic between the X-ray and optical LCs within  $1 \sigma$ .  $T_a$  from W07 fitting appears as a vertical line, denoted in bright red for X-ray and bright blue for the optical both in the middle and lower panels.

For the corrected Gold sample,  $\sigma_{int}^2$  is 33% smaller than the Gold sample without this correction for W07 and it is 12% in the case of the BPL.

Comparing between the 2- and 3D optical correlations, the total uncorrected sample for 3D has a  $\sigma_{int}^2$  33% smaller than the corresponding 2D correlation. Similarly, the 3D correlation corrected for selection biases has a  $\sigma_{int}^2$  36%

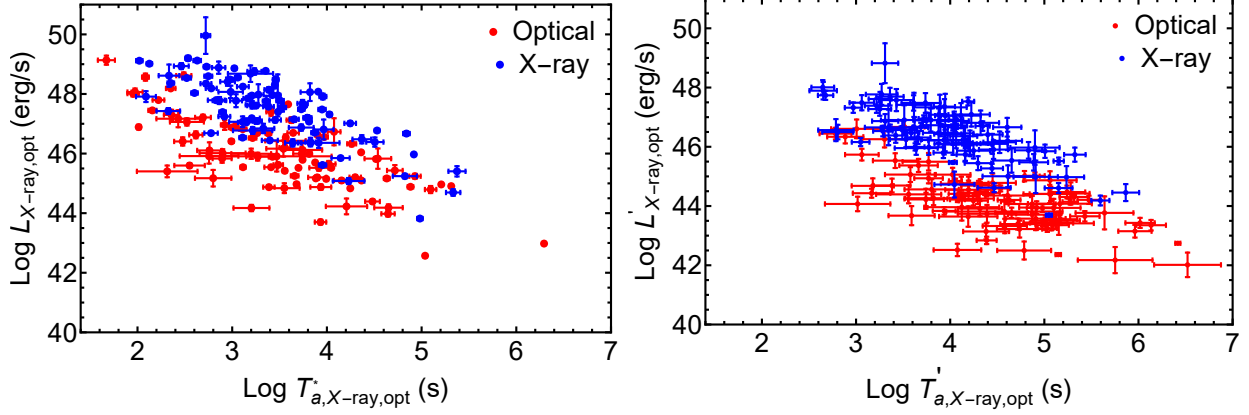


**Figure 7.** Left panel: plot of  $L_X$  and  $L_{opt}$  vs.  $T_{X,a}^*$  and  $T_{opt,a}^*$  in X-ray (blue) and optical (red). Right panel: same plot corrected for evolution.

smaller than the corresponding corrected 2D correlation. The 3D correlation for the corrected and uncorrected Gold sample has a  $\sigma_{int}^2$  39% and 6% smaller than the correspondent 2D correlations, respectively.

Thus, with our new definition, the Gold sample still reduces the scatter of the 3D and the 2D correlation both before and after correction for selection biases and redshift evolution. Given that the slope of each 2D correlation is nearly  $-1$ , it is implied that the plateau has a fixed energy reservoir independent of a given class. This can be explained within the magnetar scenario. Additionally, we find that the  $L_{opt}^{(r)} - T_{opt}^{(*r)} - L_{peak}^{(r)}$  correlation holds regardless of GRB class and plateau angle (Table 2 and 3).

Furthermore, we find that  $T_a^*$  is achromatic between X-ray and optical observations for a sub-sample of GRBs observed in both wavelengths (Fig. 5) if we do not consider selection biases for 13 cases and 11 cases when we consider evolution. An underlying chromatic behaviour between the X-rays and optical ( $T'_a$ ) is shown regardless of correction for selection biases and redshift evolution. This investigation casts a new light in the long-standing debate whether or not the plateau is achromatic in nature. The chromaticity of the plateau between X-rays and optical is aligned with the result of GRB 090510 in which the plateau is chromatic between the *Fermi*-LAT in high-energy  $\gamma$ -rays and the X-ray observations (Dainotti et al. 2021b).

#### ACKNOWLEDGMENTS

This work made use of data supplied by the UK Swift Science Data Centre at the University of Leicester. We are particularly grateful to Y. Niino for his precious discussion on the observability and limiting luminosity of the Tomo-e Gozen. We are particularly grateful to T. Sakamoto for the suggestions on the structure of the paper. We thank G. Sarracino for his help in modifying our host extinction code in Python and perform some of the fitting, J. Oseka, G. Kręzel, Z. Kania, S. Gupta and E. Johnson for data gathering, A. Rabęda, and D. Zhou for the fitting of some GRB LCs, and B. Simone for help with conversions. D.A.K. acknowledges support from Spanish National Research Project RTI2018-098104-J-I00 (GRBPhot). SY and NO acknowledge the support by the United States Department of Energy in funding the Science Undergraduate Laboratory Internship (SULI) program. We thank E. Cuellar for his work in managing the SULI summer program. SY gratefully acknowledges the support of the Vagelos Challenge Award at the University of Pennsylvania. RLB acknowledges support from the DGAPA/UNAM IG100820 and the DGAPA/UNAM postdoctoral fellowship. NF acknowledges support from the DGAPA/UNAM IN106521. Some of the data used in this paper were acquired with the RATIR instrument, funded by the University of California and NASA Goddard Space Flight Center, and the 1.5-meter Harold L. Johnson telescope at the Observatorio Astronómico Nacional on the Sierra de San Pedro Mártir, operated and maintained by the Observatorio Astronómico Nacional and the Instituto de Astronomía of the Universidad Nacional Autónoma de México. Operations are partially funded by the Universidad Nacional Autónoma de México (DGAPA/PAPIIT IG100414, IT102715, AG100317, IN109418, IG100820, IN106521 and IN105921). We acknowledge the contribution of Leonid Georgiev and Neil Gehrels to the development of RATIR. MF, LZ and AZ thank the support from the Scientific Caribbean Foundation. ES thanks the support from the Latino Education Advancement Foundation.

*Software:* dustmaps (Green 2018), astroquery (Ginsburg et al. 2019)



## REFERENCES

- Abbott, B. P., Abbott, R., Abbott, T. D., et al. Gravitational Waves and Gamma-Rays from a Binary Neutron Star Merger: GW170817 and GRB 170817A. *ApJL*, 848(2):L13, 2017a. <https://doi.org/10.3847/2041-8213/aa920c>.
- Abbott, B. P., Abbott, R., Abbott, T. D., et al. Multi-messenger Observations of a Binary Neutron Star Merger. *ApJL*, 848(2):L12, 2017b. <https://doi.org/10.3847/2041-8213/aa91c9>.
- Ahumada, T., Singer, L. P., Anand, S., et al. Discovery and confirmation of the shortest gamma-ray burst from a collapsar. *Nature Astronomy*, 2021. <https://doi.org/10.1038/s41550-021-01428-7>.
- Avni, Y. Energy spectra of X-ray clusters of galaxies. *ApJ*, 210:642–646, 1976. <https://doi.org/10.1086/154870>.
- Beskin, G., Karpov, S., Bondar, S., et al. Fast Optical Variability of a Naked-eye Burst—Manifestation of the Periodic Activity of an Internal Engine. *ApJL*, 719(1):L10–L14, 2010. <https://doi.org/10.1088/2041-8205/719/1/L10>.
- Bessell, M. S., Castelli, F., and Plez, B. Model atmospheres broad-band colors, bolometric corrections and temperature calibrations for O - M stars. *A&A*, 333:231–250, 1998.
- Blake, C. H., Bloom, J. S., Starr, D. L., et al. An infrared flash contemporaneous with the  $\gamma$ -rays of GRB 041219a. *Nature*, 435(7039):181–184, 2005. <https://doi.org/10.1038/nature03520>.
- Bloom, J. S., Frail, D. A., and Sari, R. The Prompt Energy Release of Gamma-Ray Bursts using a Cosmological k-Correction. *AJ*, 121(6):2879–2888, 2001. <https://doi.org/10.1086/321093>.
- Cannizzo, J. K. and Gehrels, N. A New Paradigm for Gamma-ray Bursts: Long-term Accretion Rate Modulation by an External Accretion Disk. *ApJ*, 700(2):1047–1058, 2009. <https://doi.org/10.1088/0004-637X/700/2/1047>.
- Cannizzo, J. K., Troja, E., and Gehrels, N. Fall-back Disks in Long and Short Gamma-Ray Bursts. *ApJ*, 734(1):35, 2011. <https://doi.org/10.1088/0004-637X/734/1/35>.
- Cano, Z., Wang, S.-Q., Dai, Z.-G., and Wu, X.-F. The Observer’s Guide to the Gamma-Ray Burst Supernova Connection. *Advances in Astronomy*, 2017:8929054, 2017. <https://doi.org/10.1155/2017/8929054>.
- Cardone, V. F., Capozziello, S., and Dainotti, M. G. An updated gamma-ray bursts Hubble diagram. *Monthly Notices of the Royal Astronomical Society*, 400(2):775–790, 2009.
- Cardone, V. F., Dainotti, M. G., Capozziello, S., and Willingale, R. Constraining cosmological parameters by gamma-ray burst X-ray afterglow light curves. *Monthly Notices of the Royal Astronomical Society*, 408(2):1181–1186, 2010.
- Costa, E., Frontera, F., Heise, J., et al. Discovery of an X-ray afterglow associated with the  $\gamma$ -ray burst of 28 February 1997. *Nature*, 387(6635):783–785, 1997. <https://doi.org/10.1038/42885>.
- Dai, Z. G. and Lu, T. Gamma-ray burst afterglows and evolution of postburst fireballs with energy injection from strongly magnetic millisecond pulsars. *A&A*, 333:L87–L90, 1998.
- Dainotti, M. G., Cardone, V. F., and Capozziello, S. A time-luminosity correlation for  $\gamma$ -ray bursts in the X-rays. *MNRAS*, 391(1):L79–L83, 2008. <https://doi.org/10.1111/j.1745-3933.2008.00560.x>.
- Dainotti, M. G. and Del Vecchio, R. Gamma Ray Burst afterglow and prompt-afterglow relations: An overview. *NewAR*, 77:23–61, 2017. <https://doi.org/10.1016/j.newar.2017.04.001>.
- Dainotti, M. G., Del Vecchio, R., Shigehiro, N., and Capozziello, S. Selection Effects in Gamma-Ray Burst Correlations: Consequences on the Ratio between Gamma-Ray Burst and Star Formation Rates. *ApJ*, 800(1):31, 2015. <https://doi.org/10.1088/0004-637X/800/1/31>.
- Dainotti, M. G., Hernandez, X., Postnikov, S., et al. A Study of the Gamma-Ray Burst Fundamental Plane. *ApJ*, 848(2):88, 2017a. <https://doi.org/10.3847/1538-4357/aa8a6b>.
- Dainotti, M. G., Lenart, A. L., Fraija, N., et al. Closure relations during the plateau emission of Swift GRBs and the fundamental plane. *Publications of the Astronomical Society of Japan*, 73(4):970–1000, 2021a. ISSN 0004-6264. <https://doi.org/10.1093/pasj/psab057>.
- Dainotti, M. G., Lenart, A. L., Sarracino, G., et al. The X-Ray Fundamental Plane of the Platinum Sample, the Kilonovae, and the SNe Ib/c Associated with GRBs. *ApJ*, 904(2):97, 2020a. <https://doi.org/10.3847/1538-4357/abbe8a>.
- Dainotti, M. G., Livermore, S., Kann, D. A., et al. The Optical Luminosity-Time Correlation for More than 100 Gamma-Ray Burst Afterglows. *ApJL*, 905(2):L26, 2020b. <https://doi.org/10.3847/2041-8213/abcda9>.
- Dainotti, M. G., Nagataki, S., Maeda, K., et al. A study of gamma ray bursts with afterglow plateau phases associated with supernovae. *A&A*, 600:A98, 2017b. <https://doi.org/10.1051/0004-6361/201628384>.



- Dainotti, M. G., Omodei, N., Srinivasaragavan, G. P., et al. On the Existence of the Plateau Emission in High-energy Gamma-Ray Burst Light Curves Observed by Fermi-LAT. *ApJS*, 255(1):13, 2021b. <https://doi.org/10.3847/1538-4365/abfe17>.
- Dainotti, M. G., Petrosian, V., Singal, J., and Ostrowski, M. Determination of the Intrinsic Luminosity Time Correlation in the X-Ray Afterglows of Gamma-Ray Bursts. *ApJ*, 774(2):157, 2013. <https://doi.org/10.1088/0004-637X/774/2/157>.
- Dainotti, M. G., Postnikov, S., Hernandez, X., and Ostrowski, M. A Fundamental Plane for Long Gamma-Ray Bursts with X-Ray Plateaus. *ApJL*, 825(2):L20, 2016. <https://doi.org/10.3847/2041-8205/825/2/L20>.
- Dainotti, M. G., Willingale, R., Capozziello, S., et al. Discovery of a Tight Correlation for Gamma-ray Burst Afterglows with “Canonical” Light Curves. *ApJL*, 722(2):L215–L219, 2010. <https://doi.org/10.1088/2041-8205/722/2/L215>.
- Dall’Osso, S., Stratta, G., Guetta, D., et al. Gamma-ray bursts afterglows with energy injection from a spinning down neutron star. *A&A*, 526:A121, 2011. <https://doi.org/10.1051/0004-6361/201014168>.
- Dichiara, S., Troja, E., Beniamini, P., et al. Evidence of Extended Emission in GRB 181123B and Other High-redshift Short GRBs. *ApJL*, 911(2):L28, 2021. <https://doi.org/10.3847/2041-8213/abf562>.
- Duncan, R. C. and Thompson, C. Formation of Very Strongly Magnetized Neutron Stars: Implications for Gamma-Ray Bursts. *ApJL*, 392:L9, 1992. <https://doi.org/10.1086/186413>.
- Efron, B. and Petrosian, V. A Simple Test of Independence for Truncated Data with Applications to Redshift Surveys. *ApJ*, 399:345, 1992. <https://doi.org/10.1086/171931>.
- Evans, P. A., Beardmore, A. P., Page, K. L., et al. Methods and results of an automatic analysis of a complete sample of Swift-XRT observations of GRBs. *MNRAS*, 397(3):1177–1201, 2009. <https://doi.org/10.1111/j.1365-2966.2009.14913.x>.
- Evans, P. A., Willingale, R., Osborne, J. P., et al. The Swift Burst Analyser. I. BAT and XRT spectral and flux evolution of gamma ray bursts. *A&A*, 519:A102, 2010. <https://doi.org/10.1051/0004-6361/201014819>.
- Fraija, N., Betancourt Kamenetskaia, B., Dainotti, M. G., et al. Afterglow light curves of the non-relativistic ejecta mass in a stratified circumstellar medium. *arXiv e-prints*, arXiv:2006.04049, 2020.
- Fukugita, M., Ichikawa, T., Gunn, J. E., et al. The Sloan Digital Sky Survey Photometric System. *AJ*, 111:1748, 1996. <https://doi.org/10.1086/117915>.
- Gehrels, N., Ramirez-Ruiz, E., and Fox, D. B. Gamma-Ray Bursts in the Swift Era. *ARA&A*, 47(1):567–617, 2009. <https://doi.org/10.1146/annurev.astro.46.060407.145147>.
- Gendre, B., Joyce, Q. T., Orange, N. B., et al. Can we quickly flag ultra-long gamma-ray bursts? *Monthly Notices of the Royal Astronomical Society*, 486(2):2471–2476, 2019. ISSN 0035-8711. <https://doi.org/10.1093/mnras/stz1036>.
- Gendre, B., Stratta, G., Atteia, J. L., et al. The Ultra-long Gamma-Ray Burst 111209A: The Collapse of a Blue Supergiant? *ApJ*, 766(1):30, 2013. <https://doi.org/10.1088/0004-637X/766/1/30>.
- Genet, F., Daigne, F., and Mochkovitch, R. Can the early X-ray afterglow of gamma-ray bursts be explained by a contribution from the reverse shock? *MNRAS*, 381(2):732–740, 2007. <https://doi.org/10.1111/j.1365-2966.2007.12243.x>.
- Ginsburg, A., Sipőcz, B. M., Brasseur, C. E., et al. astroquery: An Astronomical Web-querying Package in Python. *AJ*, 157:98, 2019. <https://doi.org/10.3847/1538-3881/aafc33>.
- Green, G. M. dustmaps: A Python interface for maps of interstellar dust. *The Journal of Open Source Software*, 3(26):695, 2018. <https://doi.org/10.21105/joss.00695>.
- Greiner, J., Mazzali, P. A., Kann, D. A., et al. A very luminous magnetar-powered supernova associated with an ultra-long  $\gamma$ -ray burst. *Nature*, 523(7559):189–192, 2015. <https://doi.org/10.1038/nature14579>.
- Heise, J., Zand, J. I., Kippen, R. M., and Woods, P. M. X-Ray Flashes and X-Ray Rich Gamma Ray Bursts. In E. Costa, F. Frontera, and J. Hjorth, editors, *Gamma-ray Bursts in the Afterglow Era*, page 16. 2001. [https://doi.org/10.1007/10853853\\_4](https://doi.org/10.1007/10853853_4).
- Hjorth, J., Sollerman, J., Møller, P., et al. A very energetic supernova associated with the  $\gamma$ -ray burst of 29 March 2003. *Nature*, 423:847–850, 2003. <https://doi.org/10.1038/nature01750>.
- Huang, K. Y., Urata, Y., Kuo, P. H., et al. Multicolor Shallow Decay and Chromatic Breaks in the GRB 050319 Optical Afterglow. *The Astrophysical Journal*, 654(1):L25–L28, 2006. ISSN 1538-4357. <https://doi.org/10.1086/510737>.
- Kann, D. A., Klose, S., and Zeh, A. Signatures of Extragalactic Dust in Pre-Swift GRB Afterglows. *ApJ*, 641(2):993–1009, 2006. <https://doi.org/10.1086/500652>.

- Kann, D. A., Klose, S., Zhang, B., et al. The Afterglows of Swift-era Gamma-ray Bursts. I. Comparing pre-Swift and Swift-era Long/Soft (Type II) GRB Optical Afterglows. *ApJ*, 720(2):1513–1558, 2010. <https://doi.org/10.1088/0004-637X/720/2/1513>.
- Kann, D. A., Klose, S., Zhang, B., et al. The Afterglows of Swift-era Gamma-Ray Bursts. II. Type I GRB versus Type II GRB Optical Afterglows. *ApJ*, 734(2):96, 2011. <https://doi.org/10.1088/0004-637X/734/2/96>.
- Kann, D. A., Schady, P., Olivares, E. F., et al. The optical/NIR afterglow of GRB 111209A: Complex yet not unprecedented. *A&A*, 617:A122, 2018. <https://doi.org/10.1051/0004-6361/201731292>.
- Kann, D. A., Schady, P., Olivares, E. F., et al. Highly luminous supernovae associated with gamma-ray bursts. I. GRB 111209A/SN 2011kl in the context of stripped-envelope and superluminous supernovae. *A&A*, 624:A143, 2019. <https://doi.org/10.1051/0004-6361/201629162>.
- Kelley, K. and Maxwell, S. Sample Size for Multiple Regression: Obtaining Regression Coefficients That Are Accurate, Not Simply Significant. *Psychol Methods*, 3(305):21, 2003. <https://doi.org/doi.org/10.1037/1082-989X.8.3.305>.
- Kouveliotou, C., Meegan, C. A., Fishman, G. J., et al. Identification of two classes of gamma-ray bursts. *The Astrophysical Journal*, 413:L101–L104, 1993.
- Kumar, P., Narayan, R., and Johnson, J. L. Mass fall-back and accretion in the central engine of gamma-ray bursts. *MNRAS*, 388(4):1729–1742, 2008. <https://doi.org/10.1111/j.1365-2966.2008.13493.x>.
- Levan, A., Jakobsson, P., Hurkett, C., et al. A case of mistaken identity? GRB 060912A and the nature of the long–short GRB divide. *Monthly Notices of the Royal Astronomical Society*, 378(4):1439–1446, 2007.
- Levan, A. J., Tanvir, N. R., Starling, R. L. C., et al. A New Population of Ultra-long Duration Gamma-Ray Bursts. *ApJ*, 781(1):13, 2014. <https://doi.org/10.1088/0004-637X/781/1/13>.
- Levesque, E. M., Bloom, J. S., Butler, N. R., et al. GRB090426: the environment of a rest-frame 0.35-s gamma-ray burst at a redshift of 2.609. *MNRAS*, 401(2):963–972, 2010. <https://doi.org/10.1111/j.1365-2966.2009.15733.x>.
- Li, L., Liang, E.-W., Tang, Q.-W., et al. A Comprehensive Study of Gamma-Ray Burst Optical Emission. I. Flares and Early Shallow-decay Component. *ApJ*, 758(1):27, 2012. <https://doi.org/10.1088/0004-637X/758/1/27>.
- Li, L., Wang, Y., Shao, L., et al. A Large Catalog of Multiwavelength GRB Afterglows. I. Color Evolution and Its Physical Implication. *ApJS*, 234(2):26, 2018a. <https://doi.org/10.3847/1538-4365/aaa02a>.
- Li, L., Wu, X.-F., Huang, Y.-F., et al. A Correlated Study of Optical and X-Ray Afterglows of GRBs. *ApJ*, 805(1):13, 2015. <https://doi.org/10.1088/0004-637X/805/1/13>.
- Li, L., Wu, X.-F., Lei, W.-H., et al. Constraining the Type of Central Engine of GRBs with Swift Data. *ApJS*, 236(2):26, 2018b. <https://doi.org/10.3847/1538-4365/aabaf3>.
- Liang, E.-W., Zhang, B.-B., and Zhang, B. A Comprehensive Analysis of Swift XRT Data. II. Diverse Physical Origins of the Shallow Decay Segment. *ApJ*, 670(1):565–583, 2007. <https://doi.org/10.1086/521870>.
- Lü, H.-J. and Zhang, B. A Test of the Millisecond Magnetar Central Engine Model of Gamma-Ray Bursts with Swift Data. *ApJ*, 785(1):74, 2014. <https://doi.org/10.1088/0004-637X/785/1/74>.
- Mazets, E., Golenetskii, S., Il’Inskii, V., et al. Catalog of cosmic gamma-ray bursts from the KONUS experiment data. *Astrophysics and Space Science*, 80(1):3–83, 1981.
- McCall, M. L. On Determining Extinction from Reddening. *AJ*, 128(5):2144–2169, 2004. <https://doi.org/10.1086/424933>.
- Metzger, B. D. Lessons from the light of a neutron star merger. *Annals of Physics*, 410:167923, 2019. <https://doi.org/10.1016/j.aop.2019.167923>.
- Metzger, B. D., Giannios, D., Thompson, T. A., et al. The protomagnetar model for gamma-ray bursts. *MNRAS*, 413(3):2031–2056, 2011. <https://doi.org/10.1111/j.1365-2966.2011.18280.x>.
- Molinari, E., Vergani, S. D., Malesani, D., et al. REM observations of GRB 060418 and GRB 060607A: the onset of the afterglow and the initial fireball Lorentz factor determination. *A&A*, 469(1):L13–L16, 2007. <https://doi.org/10.1051/0004-6361:20077388>.
- Narayan, R., Paczynski, B., and Piran, T. Gamma-ray bursts as the death throes of massive binary stars. *ApJL*, 395:L83–L86, 1992. <https://doi.org/10.1086/186493>.
- Norris, J. P. and Bonnell, J. T. Short gamma-ray bursts with extended emission. *The Astrophysical Journal*, 643(1):266, 2006.
- Norris, J. P., Gehrels, N., and Scargle, J. D. Threshold for extended emission in short gamma-ray bursts. *The Astrophysical Journal*, 717(1):411, 2010.

- Nousek, J. A., Kouveliotou, C., Grupe, D., et al. Evidence for a Canonical Gamma-Ray Burst Afterglow Light Curve in the Swift XRT Data. *ApJ*, 642(1):389–400, 2006. <https://doi.org/10.1086/500724>.
- Oates, S. R., Page, M. J., De Pasquale, M., et al. A correlation between the intrinsic brightness and average decay rate of Swift/UVOT gamma-ray burst optical/ultraviolet light curves. *MNRAS*, 426(1):L86–L90, 2012. <https://doi.org/10.1111/j.1745-3933.2012.01331.x>.
- Oates, S. R., Page, M. J., Schady, P., et al. A statistical study of gamma-ray burst afterglows measured by the Swift Ultraviolet Optical Telescope. *MNRAS*, 395(1):490–503, 2009. <https://doi.org/10.1111/j.1365-2966.2009.14544.x>.
- O’Brien, P. T., Willingale, R., Osborne, J., et al. The early X-ray emission from GRBs. *The Astrophysical Journal*, 647(2):1213, 2006.
- Paczynski, B. Are Gamma-Ray Bursts in Star-Forming Regions? *ApJL*, 494(1):L45–L48, 1998. <https://doi.org/10.1086/311148>.
- Panaiteanu, A., Mészáros, P., Burrows, D., et al. Evidence for chromatic X-ray light-curve breaks in Swift gamma-ray burst afterglows and their theoretical implications. *Monthly Notices of the Royal Astronomical Society*, 369(4):2059–2064, 2006. ISSN 1365-2966. <https://doi.org/10.1111/j.1365-2966.2006.10453.x>.
- Piro, L., Amati, L., Antonelli, L. A., et al. Evidence for a late-time outburst of the X-ray afterglow of GB970508 from BeppoSAX. *A&A*, 331:L41–L44, 1998.
- Piro, L., Troja, E., Gendre, B., et al. A Hot Cocoon in the Ultralong GRB 130925A: Hints of a POPIII-like Progenitor in a Low-Density Wind Environment. *ApJL*, 790(2):L15, 2014. <https://doi.org/10.1088/2041-8205/790/2/L15>.
- Poole, T. S., Breeveld, A. A., Page, M. J., et al. Photometric calibration of the Swift ultraviolet/optical telescope. *MNRAS*, 383(2):627–645, 2008. <https://doi.org/10.1111/j.1365-2966.2007.12563.x>.
- Postnikov, S., Dainotti, M. G., Hernandez, X., and Capozziello, S. Nonparametric study of the evolution of the cosmological equation of state with SNeIa, BAO, and high-redshift GRBs. *The Astrophysical Journal*, 783(2):126, 2014.
- Rea, N., Gullón, M., Pons, J. A., et al. Constraining the GRB-Magnetar Model by Means of the Galactic Pulsar Population. *ApJ*, 813(2):92, 2015. <https://doi.org/10.1088/0004-637X/813/2/92>.
- Rossi, A., Rothberg, B., Palazzi, E., et al. The peculiar short-duration GRB 200826A and its supernova. *arXiv e-prints*, arXiv:2105.03829, 2021.
- Rowlinson, A., Gompertz, B. P., Dainotti, M., et al. Constraining properties of GRB magnetar central engines using the observed plateau luminosity and duration correlation. *MNRAS*, 443(2):1779–1787, 2014. <https://doi.org/10.1093/mnras/stu1277>.
- Sakamoto, T., Hill, J., Yamazaki, R., et al. Evidence of exponential decay emission in the Swift gamma-ray bursts. *The Astrophysical Journal*, 669(2):1115, 2007.
- Sako, S., Ohsawa, R., Takahashi, H., et al. The Tomoe-Gozen wide field CMOS camera for the Kiso Schmidt telescope. In C. J. Evans, L. Simard, and H. Takami, editors, *Ground-based and Airborne Instrumentation for Astronomy VII*, volume 10702 of *Society of Photo-Optical Instrumentation Engineers (SPIE) Conference Series*, page 107020J. 2018. <https://doi.org/10.1117/12.2310049>.
- Schlafly, E. F. and Finkbeiner, D. P. Measuring Reddening with Sloan Digital Sky Survey Stellar Spectra and Recalibrating SFD. *ApJ*, 737(2):103, 2011. <https://doi.org/10.1088/0004-637X/737/2/103>.
- Schlegel, D. J., Finkbeiner, D. P., and Davis, M. Maps of Dust Infrared Emission for Use in Estimation of Reddening and Cosmic Microwave Background Radiation Foregrounds. *ApJ*, 500(2):525–553, 1998. <https://doi.org/10.1086/305772>.
- Si, S.-K., Qi, Y.-Q., Xue, F.-X., et al. The Three-parameter Correlations About the Optical Plateaus of Gamma-Ray Bursts. *ApJ*, 863(1):50, 2018. <https://doi.org/10.3847/1538-4357/aad08a>.
- Stratta, G., Dainotti, M. G., Dall’Osso, S., et al. On the Magnetar Origin of the GRBs Presenting X-Ray Afterglow Plateaus. *ApJ*, 869(2):155, 2018. <https://doi.org/10.3847/1538-4357/aadd8f>.
- Thompson, C. A Model of Gamma-Ray Bursts. *MNRAS*, 270:480, 1994. <https://doi.org/10.1093/mnras/270.3.480>.
- Troja, E., Cusumano, G., O’Brien, P. T., et al. Swift Observations of GRB 070110: An Extraordinary X-Ray Afterglow Powered by the Central Engine. *ApJ*, 665(1):599–607, 2007. <https://doi.org/10.1086/519450>.
- Usov, V. V. Millisecond pulsars with extremely strong magnetic fields as a cosmological source of gamma-ray bursts. *Nature*, 357:472–474, 1992. <https://doi.org/10.1038/357472a0>.
- van Eerten, H. Self-similar relativistic blast waves with energy injection. *MNRAS*, 442(4):3495–3510, 2014a. <https://doi.org/10.1093/mnras/stu1025>.

- van Eerten, H. J. Gamma-ray burst afterglow plateau break time-luminosity correlations favour thick shell models over thin shell models. *MNRAS*, 445(3):2414–2423, 2014b. <https://doi.org/10.1093/mnras/stu1921>.
- van Paradijs, J., Groot, P. J., Galama, T., et al. Transient optical emission from the error box of the  $\gamma$ -ray burst of 28 February 1997. *Nature*, 386(6626):686–689, 1997. <https://doi.org/10.1038/386686a0>.
- Vestrand, W. T., Wozniak, P. R., Wren, J. A., et al. A link between prompt optical and prompt  $\gamma$ -ray emission in  $\gamma$ -ray bursts. *Nature*, 435(7039):178–180, 2005. <https://doi.org/10.1038/nature03515>.
- Wang, X.-G., Zhang, B., Liang, E.-W., et al. How Bad or Good Are the External Forward Shock Afterglow Models of Gamma-Ray Bursts? *ApJS*, 219(1):9, 2015. <https://doi.org/10.1088/0067-0049/219/1/9>.
- Wang, X.-G., Zhang, B., Liang, E.-W., et al. Gamma-Ray Burst Jet Breaks Revisited. *ApJ*, 859(2):160, 2018. <https://doi.org/10.3847/1538-4357/aabc13>.
- Watson, A. M., Lee, W. H., Troja, E., et al. DDOTI: the deca-degree optical transient imager. In A. B. Peck, R. L. Seaman, and C. R. Benn, editors, *Observatory Operations: Strategies, Processes, and Systems VI*, volume 9910 of *Society of Photo-Optical Instrumentation Engineers (SPIE) Conference Series*, page 99100G. 2016. <https://doi.org/10.1117/12.2232898>.
- Willingale, R., O’Brien, P. T., Osborne, J. P., et al. Testing the Standard Fireball Model of Gamma-Ray Bursts Using Late X-Ray Afterglows Measured by Swift. *ApJ*, 662(2):1093–1110, 2007. <https://doi.org/10.1086/517989>.
- Woosley, S. E. Gamma-Ray Bursts from Stellar Mass Accretion Disks around Black Holes. *ApJ*, 405:273, 1993a. <https://doi.org/10.1086/172359>.
- Woosley, S. E. Gamma-Ray Bursts from Stellar Mass Accretion Disks around Black Holes. *ApJ*, 405:273, 1993b. <https://doi.org/10.1086/172359>.
- Woosley, S. E. and Bloom, J. S. The Supernova Gamma-Ray Burst Connection. *ARA&A*, 44(1):507–556, 2006. <https://doi.org/10.1146/annurev.astro.43.072103.150558>.
- Zaninoni, E., Bernardini, M. G., Margutti, R., et al. Gamma-ray burst optical light-curve zoo: comparison with X-ray observations. *A&A*, 557:A12, 2013. <https://doi.org/10.1051/0004-6361/201321221>.
- Zhang, B., Fan, Y. Z., Dyks, J., et al. Physical Processes Shaping Gamma-Ray Burst X-Ray Afterglow Light Curves: Theoretical Implications from the Swift X-Ray Telescope Observations. *ApJ*, 642(1):354–370, 2006. <https://doi.org/10.1086/500723>.
- Zhang, B. and Mészáros, P. Gamma-Ray Burst Afterglow with Continuous Energy Injection: Signature of a Highly Magnetized Millisecond Pulsar. *ApJL*, 552(1):L35–L38, 2001. <https://doi.org/10.1086/320255>.
- Zhang, B. and Meszaros, P. An Analysis of Gamma-Ray Burst Spectral Break Models. 581(2):1236–1247, 2002. <https://doi.org/10.1086/344338>.
- Zhang, B., Zhang, B.-B., Virgili, F. J., et al. Discerning the Physical Origins of Cosmological Gamma-ray Bursts Based on Multiple Observational Criteria: The Cases of  $z = 6.7$  GRB 080913,  $z = 8.2$  GRB 090423, and Some Short/Hard GRBs. *ApJ*, 703(2):1696–1724, 2009. <https://doi.org/10.1088/0004-637X/703/2/1696>.
- Zhang, B. B., Liu, Z. K., Peng, Z. K., et al. A peculiar short-duration gamma-ray burst from massive star core collapse. *Nature Astronomy*, 2021. <https://doi.org/10.1038/s41550-021-01395-z>.